Doctoral Thesis reviewed

by Ritsumeikan University

Indirect signature of Kaluza–Klein dark matter

（カルツァ・クライン暗黒物質由来の間接的信号）

March 2016

2016 年 3 月

Doctoral Program in Advanced Mathematics and Physics
Graduate School of Science and Engineering
Ritsumeikan University
立命館大学大学院理工学研究科
基礎理工学専攻博士課程後期課程

TSUCHIDA Satoshi
土田　怜

Supervisor: Professor MORI Masaki
研究指導教員：森　正樹　教授

Abstract

The lightest Kaluza–Klein particle (LKP), which appears in the theory of universal extra dimensions, is one of good candidates for cold dark matter (CDM). When LKP pairs annihilate around the center of the Galaxy where CDM is concentrated, there are some modes which produce high-energy gamma rays, electrons and positrons as final products, and we categorize them into two components. One of them is the "Line" component, which directly annihilates into $\gamma\gamma$ pair as gamma–ray products, and electron–positron pair as electron and positron products. The line component from LKP annihilation would not be helicity-suppressed, unlike in the case of neutralino signals expected by supersymmetric theory. Another one is the "Continuum" component, which consists of secondarily produced gamma rays, electrons and positrons via some decay modes. We assume the LKP mass is in the range from a few 100 GeV to 1000 GeV. We calculate the gamma-ray and electron plus positron fluxes and we analyze the resulting spectra. If we can detect the characteristic structure of these spectra, we will obtain the indirect evidence that dark matter is made of LKP. In this paper, we investigate the observability of such signals based on observational data obtained by recent measurements.

The results from analysis of gamma-ray spectrum show that if the energy resolution of a detector is 2% or worse, the characteristic peak structure caused by the line component may be diffused, and immersed in the continuum component. In addition, we can set constraints on the boost factor of dark matter concentration in the Galactic halo. By considering the electron plus positron spectrum and fitting the result of positron fraction data obtained by AMS-02 observation, the boost factor can be estimated in the range from about 30 to 300, depending on LKP mass. By using these values to compare the electron plus positron flux from LKP annihilation with recent observational data, the results indicate the light LKP, such as 300 GeV, may be excluded, since the edge-like structure has not been observed yet. However, the upper limit on the boost factor (from 4 to 26) obtained by analysis of HESS observational data may reject the boost factor derived from positron fraction fit to the AMS–02 data at 100 GeV, if the value of the boost factor is common everywhere in the Galactic halo. In this case, it implies that LKP would not be a suitable candidate of the Galactic dark matter to explain the positron fraction. On the other hand, by analyzing the gamma-ray spectrum, the upper limit on the boost factor is about 3×10^4

for 800 GeV LKP mass taking account of energy range around peak only. In the case for light LKP mass and high energy resolution, the limit may go down to about 2 taking the whole energy region into account. Thus, these constraints can be regarded as comparable with the results of analysis based on the HESS data.

The observational data for the TeV or higher energy region are still limited, and the possible LKP signal is not conclusive. Thus, we expect near-future missions with better sensitivity will clarify whether the LKP dark matter should exist or not.

Contents

1 Introduction **1**

2 The estimation for the relic density of CDM **8**

3 Searches for Dark Matter **11**
3.1 Collider search 11
3.2 Direct detection 12
3.3 Indirect detection 13

4 The theory of Extra Dimensions **16**

5 The gamma-ray signal **19**
5.1 The effect of energy resolution 23
5.2 Constraints on the boost factor: Gamma–ray 27

6 The electron and positron signal **35**
6.1 The effect of propagation 36
6.1.1 The energy loss function for electron and positron in the Galaxy 37
6.1.2 The effect of propagation in the concrete case 39
6.2 Constraints on the boost factor: Electron and Positron 42

7 Discussion **48**

8 Conclusion **52**

Acknowledgments **54**

1 Introduction

At present, most of the matter in the Universe is believed to be dark. The existence of non-luminous matter, so-called dark matter, was suggested by F. Zwicky in 1933 [1]. It was called as the "Missing mass" problem. Zwicky pointed out the velocity dispersion of the galaxies in the Coma Cluster was larger than that would be expected by assuming that the galaxies have the same ratio of mass M to luminosity L as that of the Sun, namely $M/L = M_\odot/L_\odot$ where $M_\odot$ and $L_\odot$ are the mass and luminosity of the Sun, respectively. This means that the existence of high amount of non-luminous matter is necessary to explain the result. Then the missing mass problem turned to the "dark matter" problem.

The clear and direct evidence for existence of dark matter is obtained by observations of rotation curves of galaxies. A rotation curve is given as a graph of circular velocities of ingredients of a galaxy, such as stars and gas, as a function of their distance from the galactic center. The rotation curves obtained by observation usually show a flat behavior at large distance [2]. The circular velocity moving at a radius r in Newtonian dynamics could be given as

$$v(r) = \sqrt{\frac{GM(r)}{r}} \tag{1}$$

where $M(r) = 4\pi \int_0^r \rho(r') r'^2 dr'$, and $\rho(r)$ is the mass density. The velocity $v(r)$ is expected to be proportional to $r^{-1/2}$ beyond the optical disk, because we may expect that there is no matter in that region. However, the fact that the observational data show the flat $v(r)$ curves, as shown in Fig. 1 [3], implies $M(r) \propto r$, so there must be matter beyond the optical disk, which means the existence of dark matter. The dark matter problem is one of the most important mysteries in cosmology and particle physics [4]. Since the existence of dark matter is implied, various observational data have added indirect evidences supporting the existence of dark matter, and many experiments using various methods have been planned and executed, but the nature of dark matter is still unknown.

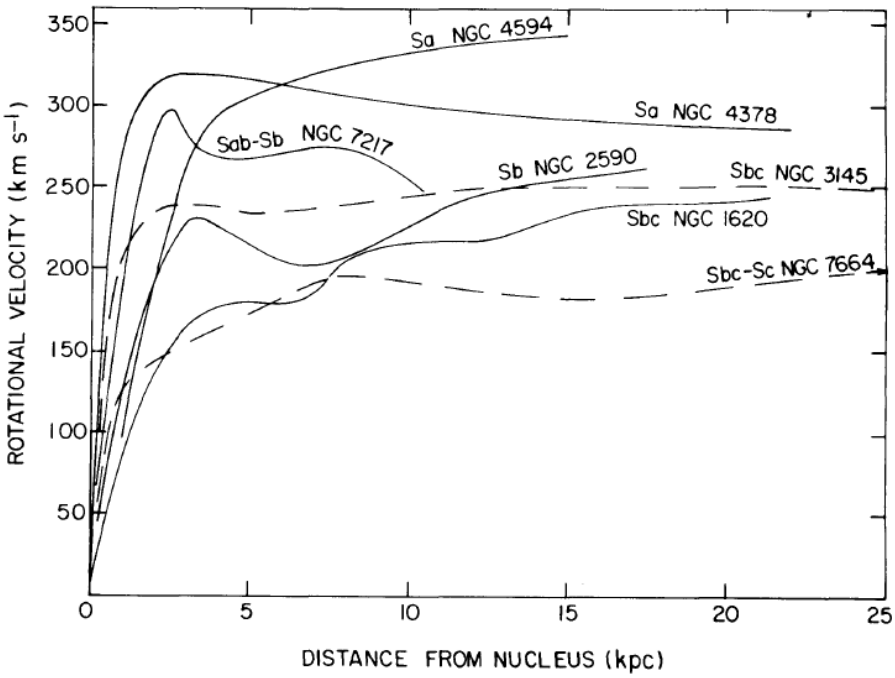

Figure 1: Rotational velocities for seven galaxies, as a function of the distance from the galactic center [3].

One of the solution to explain some of the observational results as mentioned above is to employ the "Modified Newtonian Dynamics" (MOND) [5]. However, by some discussions (see, e.g. Ref. [6]), it is realized that it is not favored to explain or replace the dark matter. As other candidate for dark matter, "Massive Astrophysical Compact Halo Objects" (MACHOs), such as neutron stars, black holes, white and brown dwarfs, have been also suggested and their observational imprints have been explored. MACHOs can account for about 20% of the dark matter in the Galaxy, and a halo model, which entirely consists of MACHOs, is ruled out at the 95% confidence level [7]. In addition, the Planck observational data, which gives $\Omega_{\rm B}h^2 = 0.02214 \pm 0.00024$ [8] where $\Omega_{\rm B}$ is the baryon density parameter of the Universe expressed as a fraction of the critical density for a flat universe, and h is the Hubble constant in units of 100 km s^{-1} Mpc^{-1}, and the theory of Big Bang Nucleosynthesis (BBN), indicate the baryonic matter could not supply the matter density required to solve the dark matter problem. Thus,

dark matter should be made of non-baryonic matter.

Dark matter should be electorically neutral and colorless, and have a very weak coupling constant with particles in the standard model. In the standard model of particle physics, only neutrino is the particle which satisfies these natures. Note that neutrino in the standard model is treated as a massless particle. However, by the observation of oscillation of atmospheric neutrinos, it is realized that the neutrino is not massless particle [9]. Then, massive neutrino could be a candidate of dark matter. Neutrinos had relativistic velocity in the early Universe, and is a candidate of so–called "Hot Dark Matter" (HDM). By cosmological simulations, neutrino dominant Universe would be ruled out [10]. On the other hand, "Cold Dark Matter" (CDM), where *Cold* implies it had non-relativistic velocity at the freeze out time in the early Universe, can explain observations of large scale structure (see, e.g. a review [11]). Then, new theories beyond the standard model, which introduce new particles corresponding to CDM, are needed.

Various kinds of electorically neutral particles predicted by theories beyond the standard model, which have not yet been detected, can be candidates for dark matter [12]. Some of feasible candidates are classified as weakly interacting massive particles (WIMPs). WIMPs are good candidates for CDM. By the Planck observational data, the density of CDM is given by $\Omega_{\rm CDM}h^2 = 0.1187 \pm 0.0017$ [8], where $\Omega_{\rm CDM}$ is the CDM density parameter of the Universe expressed as a fraction of the critical density for a flat universe. The relic density of CDM in the present Universe is determined by the annihilation cross section. If it is the order of the weak interaction, as is expected for WIMPs, the relic density could be the right order to be dark matter.

One of the theories to predict WIMP candidates is the supersymmetric theory (SUSY) [13]. In SUSY, some particles called as neutralino, gravitino and sneutrino could be WIMPs. Here, gravitino and sneutrino are the superpartners of graviton and neutrino, respectively. Neutralino is an electrically neutral, and spin 1/2 particle, and is the mixture of superpartners of photon, Z^0 boson and Higgs bosons. The lightest supersymmmetric particle (LSP) in SUSY is expected to be stable due to the conservation of R-parity, P_R, which is defined as (see, e.g. Ref. [14])

$$P_R = (-1)^{3(B-L)+2s} \tag{2}$$

where B, L are the baryon number and lepton number, respectively, and s is the spin of the particle. For particles in the standard model, P_R equals to one,

on the other hand, for the supersymmetric particles, $P_R = -1$. Thus, neutralino, gravitino or sneutrino could be a candidate of CDM if it is LSP. However, evidences for the existence of SUSY particles have not been obtained by any experiments or observations, including recent results from LHC [15, 16].

The theory of Universal Extra dimensions (UED) is also a well-created theory to explain the CDM. UED is a popular theory beyond the standard model [17], where *universal* means that all fields in the standard model can propagate into extra dimensions. New particles predicted by this theory are called Kaluza-Klein (KK) particles. Here, we consider the theory of UED containing only one extra dimension. The extra dimension is compactified with radius R. At tree level, the KK particle mass is given by [18]

$$m^{(n)} = \sqrt{\left(\frac{n}{R}\right)^2 + m_{\rm EW}^2} \tag{3}$$

where n is a mode of the KK tower, and $m_{\rm EW}$ is a zero mode mass of an electroweak particle.

We assume that the lightest KK particle (LKP) is a feasible candidate for dark matter, and we denote it $B^{(1)}$. $B^{(1)}$ is the first KK mode of the hypercharge gauge boson. Dark matter should be electrically neutral and stable. Hence, the LKP either does not interact with the standard model particles or only weakly interacts with them. In addition, LKP should have a very small decay rate to survive for a cosmological time. This hypothesis corresponds to the LKP mass $m_{B^{(1)}}$ being in the range 0.5 TeV $\lesssim m_{B^{(1)}} \lesssim$ 1 TeV using the above value for CDM density [18].

In addition to particle physics arguments, we should consider an unknown factor which indicates the relative concentration of the dark matter in astronomical bodies compared with some benchmark distributions. Some studies based on N-body simulation, such as Navarro, Frenk, and White (NFW) [19], give the "cuspy" dark matter halo density profiles. Here "cuspy" means that the dark matter density profile has the cusp in the Galactic center.

The parameterizations for the dark matter halo density profiles are given by [20]

$$\rho(r) = \rho_{\odot,\rm DM} \left(\frac{r}{r_\odot}\right)^{-\gamma} \left[\frac{1 + \left(\frac{r}{a}\right)^\alpha}{1 + \left(\frac{r_\odot}{a}\right)^\alpha}\right]^{-(\beta-\gamma)/\alpha} \tag{4}$$

where $\rho_{\odot,\rm DM}$ is the dark matter density of the halo at the position of the Sun ($\sim$ 0.3 GeV cm^{-3}), a is the scale radius for each density profile, $r_\odot$ is the

Table 1: Parameters for the different dark matter density profiles [20].

Profile	α	β	γ	a [kpc]
NFW	1.0	3.0	1.0	20.0
BE	1.0	3.0	0.3	10.2
Moore	1.5	3.0	1.5	30.0
PISO	2.0	2.0	0.0	5.0

distance of the solar system from the Galactic center (~ 8.5 kpc), and r is the distance from the Galactic center. Details for each model are discussed in Ref. [20] and references therein. We give the values of parameters for some models in Table 1, and their plots are shown in Fig. 2. Although it is very clear that the dark matter density in the Galactic center region affects on the intensity of gamma-ray emission from that region, the density profile in this region is uncertain. In Fig. 2, the vertical line at $r \simeq 0.045$ kpc corresponds to the angular distance of 0.3° for 8.5 kpc. In this region, the dark matter density rapidly decreases with increase of radius r for cuspy halo profiles, such as NFW and Moore. If the density profile is cuspy in the Galactic center region, a gamma-ray signal around the Galactic center looks like a point source with typical gamma-ray detectors. Prada *et al.* [21] suggested that the expected effects of adiabatic compression on the dark matter near the Galactic center may play important role. The effects can enhance the dark matter density in the region, so the signal from dark matter would significantly become larger.

Then we define a "boost factor", B_f, which describes the signal enhancement from dark matter annihilation in the Galactic halo [21]. N–body simulation study given by NFW [19], for example, indicates a large B_f. The boost factor B_f is defined as following expression

$$\begin{aligned} B_f &= B_\rho \times B_{\sigma v} \\ &= \left(\frac{\langle \rho^2(l) \rangle_{\Delta V}}{\langle \rho_0^2(l) \rangle_{\Delta V}} \right) \left(\frac{\langle \sigma v \rangle}{3 \times 10^{-26} \text{ cm}^3 \text{ s}^{-1}} \right)_{\Delta V} \end{aligned} \tag{5}$$

where 3×10^{-26} cm^3 s^{-1} is the typical cross section multiplied by velocity expected for thermal production of CDM [12], the volume ΔV is a diffusion scale, and $\rho_0(l)$ is a typical CDM density profile along a line-of-sight, l. B_ρ

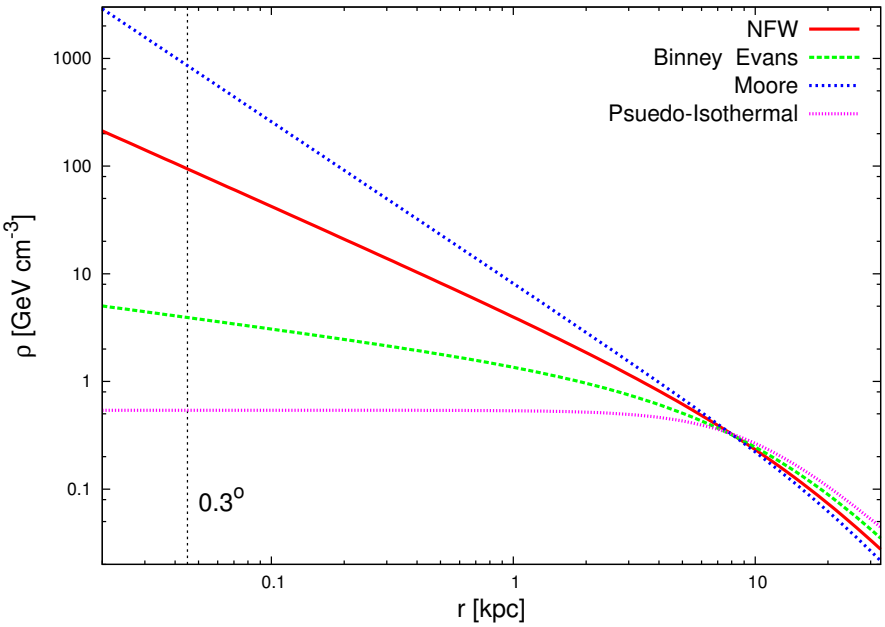

Figure 2: The dark matter mass density profiles for various halo models [20]. The vertical line at $r \simeq 0.045$ means the distance of 0.3° for 8.5 kpc.

could be as high as 1000 when taking account of the expected effects of adiabatic compression [21].

In the following, we focus on cosmic-ray observation with near-future missions, such as the Calorimetric Electron Telescope (CALET). CALET is a fine resolution calorimeter for cosmic-ray observation installed on the International Space Station in 2015 August [22]. CALET will detect gamma-rays in the energy range of 4 GeV to 1 TeV with about 1000 cm^2 effective area, and a few percent energy resolution, suitable for gamma-ray line detection [23].

This paper is organized as follows. In Section 2, we briefly review the calculation for the relic abundance of CDM by using the Boltzmann equation. In Section 3, we will mention the methods to detect or search for dark matter, and refer some results obtained by recent measurements. Then, we review the theory of extra dimensions in Section 4, and we will explain how massive scalar field with mass m in five dimensional theory is modified to that with mass $m^{(n)}$ in four dimensional point of view. In Section 5, we will analyze the gamma-ray spectral features from $B^{(1)}$ pair annihilation in the Galactic

halo taking account of the finite energy resolution of gamma-ray detector and purposefully discuss the observability of the "line" at $m_{B^{(1)}}$. We then give possible constraints on the boost factor by near-future detector from gamma-ray observations. In addition, in Section 6, we consider the total electron plus positron spectrum from LKP annihilation including the effects of propagation. Then, we calculate the positron fraction in the total flux from LKP annihilation, compare the results with recent measurements, and derive the constraints on the boost factor for the context of electron and positron observation. In Section 7, we will discuss the constraints on the boost factor by combining the gamma-ray signals and the electrons and positrons signals. We will also mention the constraints suggested by some recent literatures, and compare our results with them. The Sections 5, 6 and 7 are the original parts of our research based on Refs. [24, 25]. Finally, in Section 8, we will give the conclusion of this paper.

2 The estimation for the relic density of CDM

At present, the density of CDM is given as $\Omega_{\rm CDM}h^2 = 0.1187 \pm 0.0017$ [8]. In order to explain this value, thermally averaged annihilation cross section should take a certain value, $\langle\sigma v\rangle \sim 3 \times 10^{-26}\ {\rm cm}^3\,{\rm s}^{-1}$ [26]. In this section, we briefly review the calculation for the relic density for CDM. For more details, see e.g. [4, 26, 27].

At thermal equilibrium state, the number density for a particle χ is given by

$$n_\chi^{\rm eq} = \frac{g}{2\pi^2}\int f(\mathbf{p})\, d\mathbf{p} \tag{6}$$

where g is the number of internal degrees of freedom, and $f(\mathbf{p})$ is a Fermi-Dirac (FD) or Bose-Einstein (BE) distribution function given as

$$f(\mathbf{p}) = \frac{1}{\exp\left[\frac{\sqrt{|\mathbf{p}|^2+m_\chi^2}-\mu}{T} \pm 1\right]} \tag{7}$$

where the plus (minus) sign corresponds to FD (BE) distribution function, T is a temperature, μ is a chemical potential, m_χ is the mass of particle χ, and we take a unit of $\hbar = c = k_B = 1$. At high temperature, $T \gg m_\chi$, $n_\chi^{\rm eq}$ is proportional to T^3. On the other hand, at low temperature, $T \ll m_\chi$, that is, at non-relativistic limit, and in the Maxwell-Boltzmann approximation, $n_\chi^{\rm eq}$ drops exponentially, and it is given as

$$n_\chi^{\rm eq} \simeq g\left(\frac{m_\chi T}{2\pi}\right)^{3/2} \exp\left(-\frac{m_\chi}{T}\right). \tag{8}$$

where we assume the chemical potential μ equals to zero. When the temperature decreased below m_χ, the annihilation rate $\Gamma = n_\chi\langle\sigma v\rangle$ became smaller than the expansion rate of the Universe, H. Here $\langle\sigma v\rangle$ is the thermally averaged annihilation cross section multiplied by the relative velocity of annihilating particles. In this epoch, the particle χ cannot annihilate, and the number density per comoving volume remains fixed. To describe this quantitatively, we consider the Boltzmann equation:

$$\frac{dn_\chi}{dt} + 3Hn_\chi = -\langle\sigma v\rangle\left[(n_\chi)^2 - \left(n_\chi^{\rm eq}\right)^2\right] \tag{9}$$

If it does not include some interactions, which change the number of particles, the right-hand side would be zero, and $n_\chi \propto a^{-3}$ should be satisfied, where a is the scale factor.

Here, we solve the Eq. (9) by assuming the case that $\langle \sigma v \rangle$ does not depend on energy. In the early Universe, the expansion rate H is expressed as

$$H(T) = \sqrt{\frac{8\pi G}{3}\rho(T)} = \sqrt{\frac{4\pi^3 g_*}{45}}\frac{T^2}{M_{\rm Planck}} \tag{10}$$

where $\rho(T) = g_*\pi^2 T^4/30$ is the energy density in the early Universe, $M_{\rm Planck} = G^{-1/2} \sim 10^{19}$ GeV is the Planck mass, and g_* is the effective number of relativistic degrees of freedom. The freeze out temperature T_{FO}, when the number of particles χ is freeze out, is given by $\Gamma(T_{FO}) = H(T_{FO})$. By using typical weak scale quantities, the temperature would be given as $T_{FO} \sim m_\chi/20$ [26].

If we assume the case that entropy is not produced by some phenomena, the entropy per comoving volume in the Universe is conserved, so n_χ/s should be also constant, where $s = 2\pi^2 g_{*s} T^3/45$ is the entropy density, with g_{*s} is the number of internal degrees of freedom for entropy. By using the relations, given by Eq. (10), $\Gamma(T_{FO}) = n_\chi \langle \sigma v \rangle = H(T_{FO})$, and $T_{FO} \sim m_\chi/20$ we can obtain

$$\begin{aligned} \left(\frac{n_\chi}{s}\right)_0 &= \left(\frac{n_\chi}{s}\right)_{FO} \\ &\simeq 100 \times \left[g_*^{-1/2} g_{*s} m_\chi M_{\rm Planck} \langle \sigma v \rangle\right]^{-1} \end{aligned} \tag{11}$$

where the index "FO" means the value at freeze out, and index "0" is that at present. By employing current entropy density and the critical energy density $\rho_c \simeq 10^{-5} h^2$ GeV/cm^3, the present mass density in units of critical density is [26]

$$\Omega_\chi h^2 = \frac{m_\chi n_\chi}{\rho_c} \simeq \frac{3 \times 10^{-27} {\rm cm}^3 {\rm s}^{-1}}{\langle \sigma v \rangle} \tag{12}$$

The observational data by Planck gives $\Omega_\chi h^2 \simeq 0.1$ [8], so the cross section for the WIMPs would be given as $\langle \sigma v \rangle \simeq 3 \times 10^{-26}$ cm^3 s^{-1}. Thus, we consider the gamma–ray, electron and positron spectral features from annihilation of dark matter based on this cross section as the reference value.

In order to solve the Boltzmann equation (9) analytically, we introduce new variables

$$Y \equiv \frac{n_\chi}{s} \quad , \quad Y^{\rm eq} \equiv \frac{n_\chi^{\rm eq}}{s}. \tag{13}$$

By using a relation, $sa^3 = \text{constant}$, we can rewrite the Eq. (9) as

$$s\frac{dY}{dt} = -\langle\sigma v\rangle s^2 \left[Y^2 - (Y^{\rm eq})^2\right] \tag{14}$$

Then, by introducing a dimensionless variable $x \equiv \frac{m_\chi}{T}$, Eq. (14) is expressed as

$$\frac{dY}{dx} = -\frac{\langle\sigma v\rangle s}{Hx}\left[Y^2 - (Y^{\rm eq})^2\right], \tag{15}$$

and we approximate the cross section $\langle\sigma v\rangle$ by a non-relativistic expansion given as

$$\langle\sigma v\rangle = a + b\langle v^2\rangle + \mathcal{O}(\langle v^4\rangle) \approx a + \frac{6b}{x}. \tag{16}$$

In addition, if we set $\Delta = Y - Y^{\rm eq}$, we can obtain

$$\frac{d\Delta}{dx} = -\frac{dY^{\rm eq}}{dx} - f(x)\left[\Delta\left(\Delta + 2Y^{\rm eq}\right)\right] \tag{17}$$

where

$$f(x) = \sqrt{\frac{\pi g_*}{45}} m_\chi M_{\rm Planck}\left(a + \frac{6b}{x}\right)\frac{1}{x^2} \tag{18}$$

Then, by using the temperature T_{FO}, which is the freeze out temperature for particle χ, and introducing $x_{FO} = m_\chi/T_{FO}$, we can solve Eq. (17) for the regions $x \ll x_{FO}$ and $x \gg x_{FO}$. The solutions are given by

$$\begin{aligned} \Delta &= -\frac{dY^{\rm eq}}{dx}\frac{1}{2f(x)Y^{\rm eq}} \quad \text{for} \quad x \ll x_{FO} \\ \frac{d\Delta}{dx} &= -f(x)\Delta^2 \quad \text{for} \quad x \gg x_{FO} \end{aligned} \tag{19}$$

Here, the solution for $x \ll x_{FO}$ corresponds to the condition for quite high temperature, that is for the early Universe before the freeze out time, and the solution for $x \gg x_{FO}$ corresponds to enough after at the freeze out time. By integrating Eq. (19) from x_{FO} to ∞ and by using $\Delta_{x_{FO}} \gg \Delta_\infty$, we can derive

$$Y_\infty^{-1} = \sqrt{\frac{\pi g_*}{45}} M_{\rm Planck} m_\chi \left[\frac{a}{x_{FO}} + \frac{3b}{x_{FO}^2}\right]. \tag{20}$$

These are the standard calculation of the relic abundance for CDM.

3 Searches for Dark Matter

In this section, we briefly review the methods to hunt for dark matter, which consist of collider searches, direct and indirect dark matter (WIMP) detection being underway around the world. The collider search measures the missing energy or momentum caused by WIMPs produced in particle collisions, which escape the detector due to weakness of their interaction, The direct detection experiments search for the signals of nuclear recoil energy caused by WIMP-nuclei scatterings. The indirect detection experiments search for the spectrum and flux of standard model particle, such as photons, electrons and antiparticles, which are expected to be produced secondarily by dark matter particle annihilation or decay. These searches are independent and complementary to each other. Figure 3 shows the scheme to detect and search for WIMPs. The annihilation of dark matter (DM) particles could produce pairs of the standard model (SM) particles (upwards direction, *Indirect Detection*). On the other hand, the collisions of the SM particles, such as electrons or protons, could produce pairs of DM particles (downward direction, *Collider Search*). Then, the interactions of WIMP-nuclei scatterings can produce the direct signal of DM particles as recoil energies (horizontal direction, *Direct Detection*). To establish the nature of dark matter, we have to investigate the interactions between WIMPs and standard model particles. More detailed reviews of these topics can be found in Refs. [11, 28], for example.

3.1 Collider search

The dark matter particles (WIMPs) might be generated at the high energy colliders, such as Large Hadron Collider (LHC) [15, 16]. When the high-energy particles in the standard model collide, WIMPs are expected to be produced directly or secondarily (cascade decay). One of important tasks at collider research is to search SUSY particles. The WIMPs do not have electromagnetic interactions nor baryonic nature (colorless), and would have a weak coupling with the standard model particles, so the WIMPs could escape the detector. Thus, they give rise to a characteristic signal of missing energy or momentum. The missing energy or momentum is determined by observation of recoiled objects, such as jets, heavy quarks, leptons and photons. By investigating these signals, one can identify the mass and nature of WIMPs, and this is just the collider search for WIMPs. More detailed discussions and recent results are given in Ref. [11] and references therein,

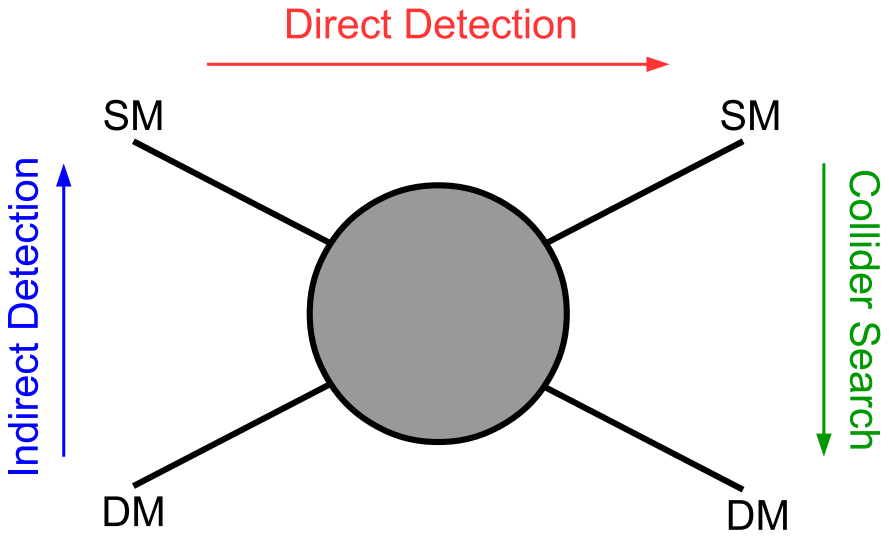

Figure 3: The schematic plot of direct detection, indirect detection and collider search for dark matter (DM). The arrows indicate the direction of the reactions.

for example.

3.2 Direct detection

To prove the existence of WIMPs, the direct detection of these particles would be the most satisfactory method. When we attempt the direct detections of dark matter, they are exposed to the background from cosmic rays, so the most of detectors are located in deep underground. The direct detection observes nuclear recoil after WIMP–nuclei elastic scattering. The cross section between WIMPs and the particles in the standard model is too small, so occurring the interactions are quite rare. This event rate should be $R \simeq n\sigma\langle v\rangle/m_N$, where $n = \rho_0/m_\chi$ is the WIMPs number density (ρ_0 and m_χ are local dark matter density and WIMPs mass, respectively), σ is the elastic scattering cross section, $\langle v\rangle$ is the average speed of WIMPs relative to the target nucleus, and m_N is a nucleus mass. The expected differential recoil energy spectrum between a WIMP with mass m_χ and a nucleus with

mass m_N is given as [26, 29]

$$\frac{dR}{dQ} = \frac{\sigma_0 \rho_0}{\sqrt{\pi} v_0 m_\chi m_r^2} F^2(Q) T(Q) \tag{21}$$

where Q is the energy deposited in the detector, σ_0 is the elastic scattering cross section between WIMP and nucleus, and $m_r = m_\chi m_N/(m_\chi + m_N)$ is the reduced mass. $F(Q)$ is the nuclear form factor, and $T(Q)$ is a dimensionless quantity integral over the local WIMP velocity distribution.

As mentioned above, the direct detection experiments search for the nuclear recoil signals caused by WIMP-nuclei scatterings. The recoil energy depends on nucleus (target) mass m_N and WIMP mass m_χ. If m_N equals to m_χ, we could detect the WIMPs most effectively, so we expect to identify the WIMP mass by utilizing various kinds of target materials. Therefore, many kinds of direct detection experiments are suggested, planned and are underway around the world. There are a number of experimental techniques, and they are classified in different groups (see e.g. Ref. [30]). For example, scintillator experiments (such as DAMA [31], KIMS [32]), cryogenic crystal experiments (such as CDMS [33], EDELWEISS [34], CoGeNT [35], CRESST [36]), noble gas or liquid experiments (such as XENON [37], ZEPLIN [38], PANDA-X [39], XMASS [40]), and metastable gas or liquid experiments (such as COUPP [41], PICASSO [42], SIMPLE [43]).

So far, the dark matter signals, which are given rise to nuclear recoil events, have not been observed yet by most of the direct detection experiments. However, some experiments report positive signals, but the results are sometimes controversial and the validity as dark matter signals are not established, one must say. For more details, see e.g. Ref. [28].

3.3 Indirect detection

Many indirect detection experiments to search for dark matter signals are planned, under-construction and ongoing. The usual method to detect dark matter signals indirectly is to search for gamma-rays, electrons, neutrinos, and charged anti-particles (such as positrons and antiprotons) produced by annihilation or decay of dark matter particles, in their concentrated region, e.g. the Galactic center.

In the Galaxy, there are complicate magnetic fields, so charged particles, such as electrons, positrons and antiprotons, will lose their source information (energies and directions) during propagation in the Galaxy. On the other

hand, neutral particles, such as gamma-rays and neutrinos, can reach to Earth retaining information of original source. There are many cosmic-ray experiments dedicated to search for dark matter annihilation or decay signals. To avoid the atmospheric blind, the instruments are usually located in space (to observe gamma rays, electrons and charged anti-particles) or in deep underground (to observe neutrinos).

Recent progress in gamma-ray observation has revealed new findings in the Galactic center region (here we concentrate discussion in the energy region above 10 GeV in our interest). A point-like high-energy gamma-ray sources at the Galactic center have been observed by HESS [44] and other ground-based experiments at energies greater than 100 GeV. Some authors argued the observed HESS signal might result from annihilation of heavy (> 10 TeV) dark matter [45], but since its spectrum is represented well by a power-law plus an exponential cut-off, it is discussed that the bulk of the emission must have non-dark matter origin [46]. The Fermi-LAT identified a GeV gamma-ray source 2FGL J1745.6-2858 [47] consistent with Sgr A*, in arcminute-scale at least above 10 GeV, in accordance to the HESS source [48]. The energy spectrum can be explained by a hadronic interaction of relativistic protons injected to a central source in a power-law plus exponential cutoff spectrum [48]. (Note, however, the energy resolution of ground-based atmospheric Cherenkov detectors like HESS is 15–20% and narrow features, if any, will be washed out: see below). Also, an enhancement of around 130 GeV in the energy spectrum of gamma-rays from the Galactic center region has been reported using the Fermi-LAT data, which may indicate a possible dark matter annihilation signal [49, 50, 51, 52]. However, the analysis by the Fermi-LAT collaboration did not confirm the significance of the line detection and the dark matter interpretation is disfavored [53, 54]. Thus the possible dark matter signal in high energy region is far from conclusive and clearly we need more sensitive observations.

In the case for indirect detection of charged particles, the sensitive measurements of electron and positron flux in the energy range up to a few 100 GeV have been executed recently by PAMELA [55], Fermi-LAT [56] and AMS-02 [57]. These observational data show the positron excess significantly at energies higher than about 10 GeV. According to recent reports, the excess of electron plus positron flux is also observed by ATIC [58] and PPB-BETS [59]. In general, as a function of energy, the contribution of the interstellar matter to the positron fraction decreases with increasing the energy, so the standard cosmic–ray propagation models in the Galaxy could

not explain the positron excess. Thus, to give a consistent explanation for observed positron excess, some additional sources producing positrons are needed. Then, if the positron excess is caused by dark matter annihilation, the dark matter particles should have a few 100 GeV. Note that extra contribution of astrophysical sources, e.g. nearby pulsars [60] and supernova remnants [61], could also explain the positron excess.

In addition, the excess of antiproton fraction (antiproton to proton ratio) is also confirmed by AMS collaboration [62]. It is an unsolved issue that the antiproton excess is caused by whether the secondary antiprotons background [63, 64] or dark matter annihilation, and further studies and experiments are necessary.

On the other hand, since neutrinos interact weakly with other particles, their energy loss and randomization of directions would be negligible. Thus, neutrinos may carry the original information of distribution and nature of dark matter particles. However, for the same reason, detecting neutrinos is more difficult compared with detecting gamma-ray or charged particles. Even so, high energy neutrinos are observed by some experiments, such as Super-Kamiokande [65], ANTARES [66] and IceCube [67, 68]. These telescopes are located in deep underground to shield cosmic-ray backgrounds. For more detailed discussions, see e.g. Ref. [69].

Some of the indirect detection experiments have reported evidences for possible existence of dark matter, i.e. excess of positrons and antiprotons. Thus, the important thing is to judge whether the obtained signals are from dark matter or not (astrophysical background).

In this paper, as mentioned above, we employ the theory of universal extra dimension (UED), and we assume the lightest Kaluza-Klein particle (LKP), which appears in UED, would be a candidate of dark matter. Then, we analyze the particle spectra expected to be obtained by indirect detection experiments.

4 The theory of Extra Dimensions

At the beginning of the 20th century, Kaluza and Klein realized the theory of extra dimensions [70, 71]. The extra dimensions are compactified into very small scale, so we have not been able to observe their existence yet. When a particle propagates in extra dimensions, we cannot see its movement, but it leaves some trails in four dimensional spacetime. Thus, we could expect new particles appear in such theory, and if there are stable particles in the theory, the particles may account for the observed dark matter. In this section, we briefly mention spirits of the theory of extra dimensions.

The new particle states can be understood easily by a following example: In four dimensions, the energy-momentum relation is given as

$$E^2 = p_{x_1}^2 + p_{x_2}^2 + p_{x_3}^2 + m^2 = \mathbf{p}^2 + m^2 \tag{22}$$

where x_1, x_2, x_3 are the three dimensional Cartesian coordinates, E and m are the energy and mass of the particle, respectively. By assuming there is only one extra dimension with coordinate y, the relation is modified as

$$E^2 = \mathbf{p}^2 + p_y^2 + m^2. \tag{23}$$

If the fifth dimension is compactified with radius R as per Fig. 4,

$$y \sim y + 2\pi R, \tag{24}$$

this periodic condition implies a quantization of momentum, which relates to the wavelength $\lambda = 2\pi R/n$, where n is a positive integer, along the direction of the extra dimension, so the momentum in fifth dimension is expressed as

$$p_y = \frac{2\pi}{\lambda} = \frac{n}{R}. \tag{25}$$

Thus, Eq. (23) is rewritten as

$$E^2 = \mathbf{p}^2 + \left(\frac{n}{R}\right)^2 + m^2 = \mathbf{p}^2 + \left(m^{(n)}\right)^2 \tag{26}$$

where $m^{(n)} = \sqrt{\left(\frac{n}{R}\right)^2 + m^2}$ is the effective mass of the particles moving in the extra dimensions.

A simple example to understand the higher dimension has been given as above, and here we provide the expression of effective mass by more precise

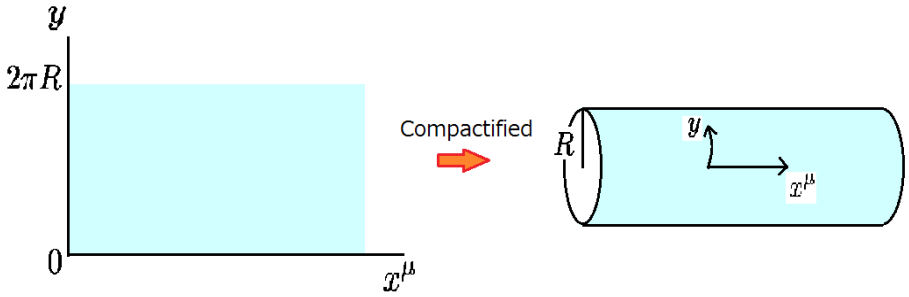

Figure 4: The compactified one extra dimension on a circle.

discussion. We assume that the theory has only one extra dimension, and the five dimensional spacetime consists of one dimensional time coordinate and four dimensional space coordinates. These coordinates are denoted as $x^M = (x^\mu, y)$, where $M = 0,\ 1,\ 2,\ 3,\ 5$, $\mu = 0,\ 1,\ 2,\ 3$, x^μ is the four-dimensional spacetime coordinates, and $y = x^5$ is the coordinate in the direction of the extra dimension, and the five dimensional metric is defined as $\eta_{MN} = \mathrm{diag}(+,-,-,-,-)$. The compactification of the extra dimension on a circle with radius R means that the points y and $y + 2\pi R$ are identical. We consider the five dimensional action for a massive scalar field $\Phi(x^\mu, y)$ with mass m given as

$$S = \int d^4x\ dy\ \frac{1}{2}\left[\partial_M \Phi^*(x^\mu, y)\partial^M \Phi(x^\mu, y) - m^2 \Phi^*(x^\mu, y)\Phi(x^\mu, y)\right]. \quad (27)$$

Since this action function must be dimensionless, the scalar field has 3/2 power of mass dimension in five dimensional theory (c.f. the scalar field has one mass dimension in four dimensional theory). The scalar field value is periodic in y coordinate direction, which corresponds to the compactified direction, so $\Phi(x^\mu, y + 2\pi R) = \Phi(x^\mu, y)$. This implies that the any function of y can be written as a form of Fourier series expansion. That is, $\Phi(x^\mu, y)$ is expanded as

$$\Phi(x^\mu, y) = \frac{1}{\sqrt{2\pi R}} \sum_{n=-\infty}^{\infty} \Phi^{(n)}(x^\mu) \mathrm{e}^{i\frac{n}{R}y} \quad (28)$$

where $\Phi^{(n)}(x^\mu)$ are the Fourier components. By substituting Eq. (28) into

Eq. (27), and by using the orthogonality relation between different modes;

$$2\pi R\,\delta_{n,l} = \int_0^{2\pi R} dy \exp\left[-i\frac{l-n}{R}y\right] \tag{29}$$

we can obtain

$$\begin{aligned} S &= \int d^4x \sum_{n=-\infty}^{\infty} \\ &\times \frac{1}{2}\left[\partial_\mu \Phi^{(n)^*}(x^\mu)\partial^\mu \Phi^{(n)}(x^\mu) - \left(\frac{n^2}{R^2} + m^2\right)\Phi^{(n)^*}(x^\mu)\Phi^{(n)}(x^\mu)\right]. \end{aligned} \tag{30}$$

Although we start with a massive scalar field $\Phi(x^\mu, y)$ with mass m in five dimension and compactified fifth dimension on a circle with radius R, we can interpret Eq. (30) from the four dimensional point of view. The action describes an infinite series of particles (Kaluza-Klein (KK) towers) with mass $m^{(n)}$:

$$m^{(n)} = \sqrt{\left(\frac{n}{R}\right)^2 + m^2}. \tag{31}$$

Of course, when n equals to zero (i.e. the "zero" mode), this situation corresponds to an ordinary massive scalar field in four dimensions with mass m. On the other hand, for $n \neq 0$, the scalar field has mass with given by Eq. (31), and the mass is derived from the derivation with respect to the extra dimension. Thus, the mass of the first KK mode assuming massless scalar field, which means $m = 0$, in five dimension will be naively $m^{(n)} = 1/R$.

The model of Universal Extra Dimensions (UED) was introduced by Appelquist, Cheng and Dobrescu [72]. In the context of UED, all standard model fields can propagate into the extra dimensions, so the momentum is conserved in extra dimensions. This corresponds to the KK number conservation, and the KK masses are given by [18]

$$m^{(n)} = \sqrt{\left(\frac{n}{R}\right)^2 + m_{\rm EW}^2}. \tag{32}$$

where $m_{\rm EW}$ is electroweak particle mass in standard model. As a result, it implies that the lightest first KK excitation of all standard model fields should be stable, that is, the lightest KK particle (LKP) will be stable. If it is a neutral particle, it can be a good candidate for dark matter.

For more detailed discussions concerning extra dimensions are given in Ref. [73] and references therein.

5 The gamma-ray signal

Here, we consider the gamma–ray emission from LKP. When LKP pairs annihilate, there are many LKP annihilation modes which contain gamma-rays as final products. These include gamma-ray "lines" from two-body decays, and "continuum" emission from decay or fragmentation of secondaries. The cross section for $B^{(1)}$ pair annihilation has been calculated [74], and we assume the mass shift between $B^{(1)}$ and KK fermions is 5% at the first KK level. In addition, branching ratios into these modes can be calculated for $B^{(1)}$ pair annihilation [17, 18, 27] and are not dependent on parameters other than $m_{B^{(1)}}$. The branching ratios are given as follows: 20% for charged leptons, 11% for up-type quarks, 0.7% for down-type quarks, 1% for charged gauge bosons, and 0.5% for neutral gauge bosons [27, 75]. This paper considers three patterns for the continuum: $B^{(1)}$ pairs annihilate into (i) quark pairs, (ii) lepton pairs ($\tau^+\tau^-$) which cascade or produce gamma-rays, or (iii) two leptons and one photon ($l^+l^-\gamma$).

The differential spectra of photons for each pattern for the continuum can be written in the following forms:

(i) *For the quark pairs*

The differential spectra of photons from the quark pairs produced by dark matter annihilation is given as [76]

$$\frac{dN_\gamma^i}{dx} = \eta\, x^a\, \mathrm{e}^{b+cx+dx^2+ex^3} \tag{33}$$

where $x = E/m_\chi$, m_χ is dark matter mass, and i identify the kind of quarks. The value of η is 2 for top quark final state, and 1 for otherwise. The values of fitting parameters, $a,\ b,\ c,\ d$ and e, are calculated by Fornengo *et al.* [76], and the parameters are given in Table 2 for the cases of $m_\chi = 500$ GeV and $m_\chi = 1000$ GeV.

(ii) *For the tauon pairs*

The differential spectra of photons from tauon pairs produced by dark matter annihilation is given as [76]

$$\frac{dN_\gamma^\tau}{dx} = x^{a_\tau}(b_\tau x + c_\tau x^2 + d_\tau x^3)\mathrm{e}^{e_\tau x} \tag{34}$$

The values of fitting parameters, $a_\tau,\ b_\tau,\ c_\tau,\ d_\tau$ and e_τ, are also calculated by Fornengo *et al.* [76], and the parameters are given in Table 3 for the cases of $m_\chi = 500$ GeV and $m_\chi = 1000$ GeV.

Table 2: Fitted Parameters of Eq. (33) for the photons from the quark pairs produced by dark matter annihilation [76].

	$m_\chi = 500$ GeV			$m_\chi = 1000$ GeV		
	u	s	t	u	s	t
a	-1.5	-1.5	-1.5	-1.5	-1.5	-1.5
b	0.047	0.093	-0.44	0.0063	0.040	-0.45
c	-8.70	-9.13	-19.50	-8.62	-8.84	-19.05
d	9.14	4.49	22.96	8.53	2.77	21.96
e	-10.30	-9.83	-16.20	-9.73	-7.71	-15.18
	d	c	b	d	c	b
a	-1.5	-1.5	-1.5	-1.5	-1.5	-1.5
b	0.047	0.25	0.48	0.0063	0.17	0.37
c	-8.70	-10.76	-16.87	-8.62	-10.23	-16.05
d	9.14	4.25	21.09	8.53	2.13	18.01
e	-10.30	-8.70	-22.49	-9.73	-7.00	-19.50

Table 3: Fitted Parameters of Eq. (34) for the photons from the tauon pairs produced by dark matter annihilation [76].

	$m_\chi = 500$GeV	$m_\chi = 1000$ GeV
a_τ	-1.34	-1.31
b_τ	6.27	6.94
c_τ	0.89	-4.93
d_τ	-4.90	-0.51
e_τ	-5.10	-4.53

(iii) *For the lepton-lepton-gamma ($l^+l^-\gamma$)*

For the process $B^{(1)}$ pairs annihilate into $l^+l^-\gamma$, the tree-level Feynman diagrams are shown in Fig. 5, which are given in Ref. [18]. The differential spectra of photons from the $l^+l^-\gamma$ produced by dark matter annihilation is

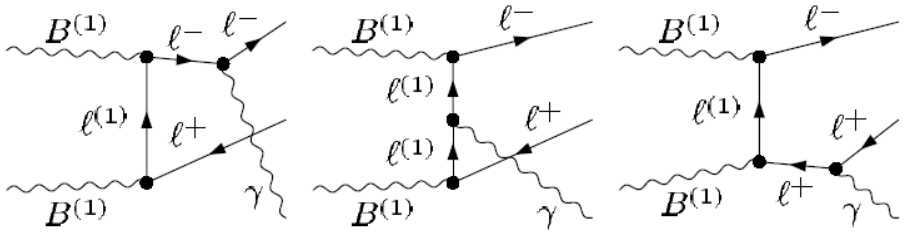

Figure 5: The tree-level Feynman diagrams which contribute to the process $B^{(1)}B^{(1)} \to l^+l^-\gamma$ as per Ref. [18].

given as [18]

$$\begin{aligned} \frac{dN_\gamma^l}{dx} &\equiv \frac{d(\sigma_{l^+l^-\gamma}v)/dx}{\sigma_{l^+l^-\gamma}v} \\ &\simeq \frac{\alpha}{\pi}\frac{(x^2-2x+2)}{x}\ln\left[\frac{m_{B^{(1)}}^2}{m_l^2}(1-x)\right] \end{aligned} \tag{35}$$

where m_l is the mass for leptons (electron, muon, tauon), and α is a fine structure constant.

The resulting gamma-ray spectra of the continuum component for $m_{B^{(1)}} =$ 800 GeV are reproduced in Fig. 6 as per Bergström *et al.* [18]. In this figure, the solid line shows the total number of photons per $B^{(1)}$ pair annihilations, the dotted, dashed and dot-dashed lines show the number of photons via quark fragmentation, via lepton fragmentation, and from the $l^+l^-\gamma$ mode, respectively, as a function of $x = E_\gamma/m_{B^{(1)}}$.

When $B^{(1)}$ pairs annihilate into photon pairs, they appear as a "line" at $m_{B^{(1)}}$ in the gamma-ray spectrum. The production cross section of this mode is approximately 130 pb for the 5% mass splitting at the first KK level [74]. This "line" feature is the most prominent signal of KK dark matter, while in some theories line models are loop-suppressed and thus usually subdominant (see, e.g. Bringmann *et al.* [77]). This study focuses on the detectability of this "line" structure by near-future detector taking account of their finite energy resolution.

The distribution of dark matter is expected to be non-uniform in the Universe, and to be concentrated in massive astronomical bodies due to gravity.

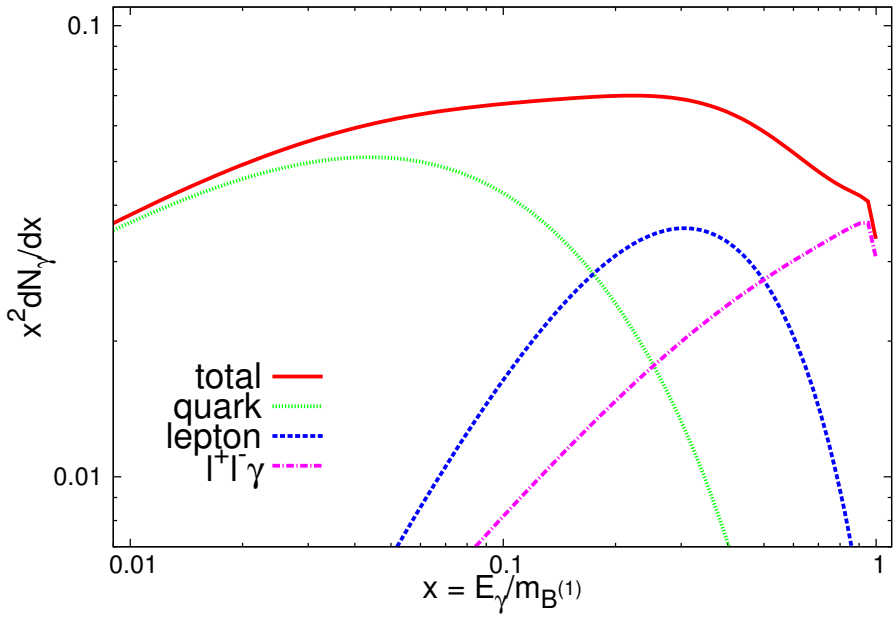

Figure 6: Gamma-ray spectra of the continuum emission. The lines show the number of photons multiplied by $x^2 = (E_\gamma/m_{B^{(1)}})^2$ as follows: the solid line shows the total number of photons per $B^{(1)}B^{(1)}$ annihilation, the dotted line shows the number via quark fragmentation, the dashed line shows the number via lepton fragmentation, and the dot-dashed line shows the number from the $l^+l^-\gamma$ component. We have assumed $m_{B^{(1)}} = 800$ GeV and mass splitting is 5% at the first KK level.

The gamma-ray flux from annihilation of dark matter particles in the Galactic halo can be written as [78]

$$\Phi_\gamma(E_\gamma, \psi) = \frac{\langle\sigma v\rangle}{8\pi M^2} \sum_i B_i \frac{dN_\gamma^i}{dE_\gamma} \int_{\rm line-of-sight} \rho^2(l) dl(\psi) \qquad (36)$$

where M is the dark matter mass, B_i is the branching ratio into the tree–level annihilation final state i, the function $\rho(l)$ is the dark matter density along the line-of-sight $l(\psi)$, where ψ is the angle with respect to the Galactic center. dN_γ^i/dE_γ is the gamma–ray spectrum generated per annihilation, and $\langle\sigma v\rangle$ is the total averaged thermal cross section multiplied by the relative velocity of particles. The value of $\langle\sigma v\rangle$ can be calculated for a given dark

matter candidate, so its uncertainty is usually small in terms of considering the cross section containing only an s-wave. However, this is not always the case, because some models have velocity-dependent cross sections [79, 80]. In addition, $\rho(l)$ is highly dependent on the substructure of the dark matter distribution in the Galactic halo along the line-of-sight.

Some constraints from observations on the KK dark matter models have been reported. The Large Area Telescope on board the Fermi Gamma-Ray Space Telescope (Fermi-LAT) team searched for gamma-ray emission from dwarf spheroidal galaxies around the Milky Way galaxy and set constraints on dark matter models with non-detection results [81]. The High Energy Stereoscopic System (HESS) array of imaging atmospheric Cherenkov telescopes observed the Sagittarius dwarf spheroidal galaxy in the sub-TeV energy region and derived a lower limit on the $m_{B^{(1)}}$ of 500 GeV [82]. These results put constraints on B_f of dark matter halo KK particles. The present limits allow the maximum value of boost factors in the range of 2–60 ($m_{B^{(1)}} = 200$ GeV) to 600–1.5×10^4 (1000 GeV) by Fermi-LAT [81], 0.8–30 (400 GeV) to 5–160 (1000 GeV) by HESS [82].

5.1 The effect of energy resolution

The gamma-ray flux $d\Phi_\gamma(\Delta\Omega)/dE_\gamma$ reaching a detector can be expressed as [18]

$$E_\gamma^2 \frac{d\Phi_\gamma(\Delta\Omega)}{dE_\gamma} = K \times B_f \times x^2 \frac{dN_\gamma}{dx}, \tag{37}$$

where $\Delta\Omega$ is the angular acceptance of the detector,

$$K \simeq 3.5 \times 10^{-8}\ \mathrm{m^{-2} s^{-1} TeV} \left(\frac{0.8\mathrm{TeV}}{m_{B^{(1)}}}\right) \times \left(\frac{\langle\sigma v\rangle_{\mathrm{LKP}}}{3 \times 10^{-26}\ \mathrm{cm^3\ s^{-1}}}\right) \langle J_{\mathrm{GC}}\rangle_{\Delta\Omega} \Delta\Omega, \tag{38}$$

where $\langle\sigma v\rangle_{\mathrm{LKP}} \simeq 3 \times 10^{-26} (0.8\ \mathrm{TeV}/m_{B^{(1)}})^2\ \mathrm{cm^3\ s^{-1}}$ is the cross section multiplied by velocity expected for thermal production of LKP [18], and $\langle J_{\mathrm{GC}}\rangle_{\Delta\Omega}$ is a dimensionless line-of-sight integral averaged over $\Delta\Omega$. If we assume an NFW profile, $\langle J_{\mathrm{GC}}\rangle_{\Delta\Omega}\Delta\Omega$ equals to 0.39 for a $\Delta\Omega = 10^{-4}$ [78], where the $\Delta\Omega$ is assumed to be reasonable value both for the angular resolution of CALET (0.2 - 0.3°) [23] and the observed localization of the Galactic center

source observed by Fermi-LAT [48]. In this case dN_γ/dx includes both the continuum and line components.

Now, we discuss the effect of energy resolution of detectors. If the measured energy dispersion for mono-energetic gamma-rays behaves as a Gaussian distribution and the energy resolution of the detector is finite, the measured gamma-ray spectrum is blurred. This effect is shown in Fig. 7 for the "continuum" component assuming the 1% energy resolution. Here we draw the curve assuming the following equation

$$g(E) \propto \int f(E') \times \exp\left[-\frac{(E-E')^2}{2\sigma_E^2}\right] dE', \tag{39}$$

where $f(E')$ corresponds to a function shown by the solid line in Fig. 6, and σ_E is the energy resolution.

Next we analyze how the "line" from the $B^{(1)}$ pair annihilation into photon pairs looks above the "continuum". In Fig. 8, the solid line shows the continuum component only with an energy resolution of 1%, and the patterned lines show "line" plus "continuum" spectra for different energy resolutions: the dotted line, dashed line and dot-dashed line show the spectra when the energy resolution is 0.5%, 1% and 2% with the Gaussian distribution respectively, assuming the boost factor $B_f = 100$. We also point out that the peak energies of the expected spectra ($E_{\rm peak}$) are 0.2% and 0.9% smaller than $m_{B^{(1)}}$, for 0.5% and 1% energy resolution, respectively. For 2% energy resolution, the peak structure is difficult to see.

To investigate the tendency of the line component quantitatively, we consider the line to continuum ratio, which is referred to as "Line fraction (LF)". LF is defined as

$$LF = \frac{\sum_i F_i^l}{\sum_i F_i^c} \tag{40}$$

where F_i^c, F_i^l are the fluxes of the continuum component and the line component of the i-th energy bin, respectively, and the energy bin width is set to 0.5 GeV. The summation runs from the lower to the upper energy limit of the observed line. This range is taken as $-3\sigma_E$ to $+3\sigma_E$ for each $m_{B^{(1)}}$, since the flux above $m_{B^{(1)}}$ drops rapidly. The result is shown in Fig. 9 as a function of $m_{B^{(1)}}$. In this figure, we can see that the value of the line fraction increases as $m_{B^{(1)}}$ becomes heavier, which implies characteristic peak structure is clearer for heavier $m_{B^{(1)}}$.

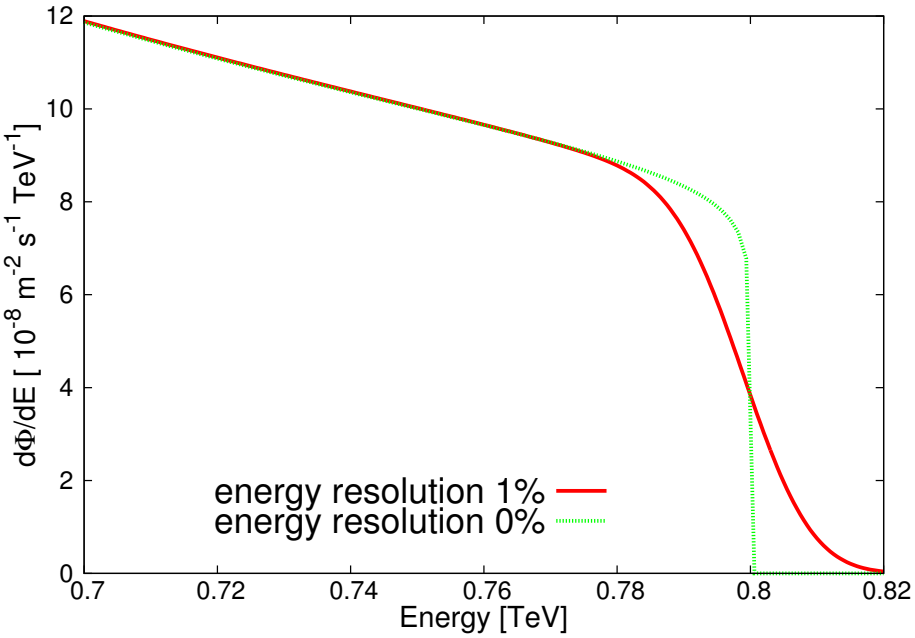

Figure 7: Gamma-ray spectrum of the continuum taking account of the energy resolution assuming $m_{B^{(1)}} = 800$ GeV. The solid line assumes an energy resolution of 1% with a Gaussian distribution, and the dotted line does not include the effect of energy resolution, as per the solid line in Fig. 6. The assumed boost factor is 100.

We can transform the spectra into counts to be observed by gamma-ray detectors. This is accomplished through multiplying by a factor of 3×10^6 m^2 s for an assumed observation time of 1 yr $= 3 \times 10^7$ s and an assumed effective area of 0.1 m^2. These values arise from the typical aforementioned CALET sensitivity [23]. When analyzing observational data, the energy bin width must be specified. Bin widths of twice as much as 0.5%, 1% and 2% of $m_{B^{(1)}}$ (about one standard deviation of energy reconstruction) was used in order to match the each energy resolution. The resulting histograms for $m_{B^{(1)}} =$ 800 GeV are shown in Fig. 10, where plots of the three cases corresponding to energy resolutions of 0.5%, 1% and 2% are shown. The figure shows that if the energy resolution of the detector becomes 2% or worse, the characteristic peak indicating the $m_{B^{(1)}}$ will be diffused, making it hard to resolve into the line and continuum components. Here, we do not consider for the systematic

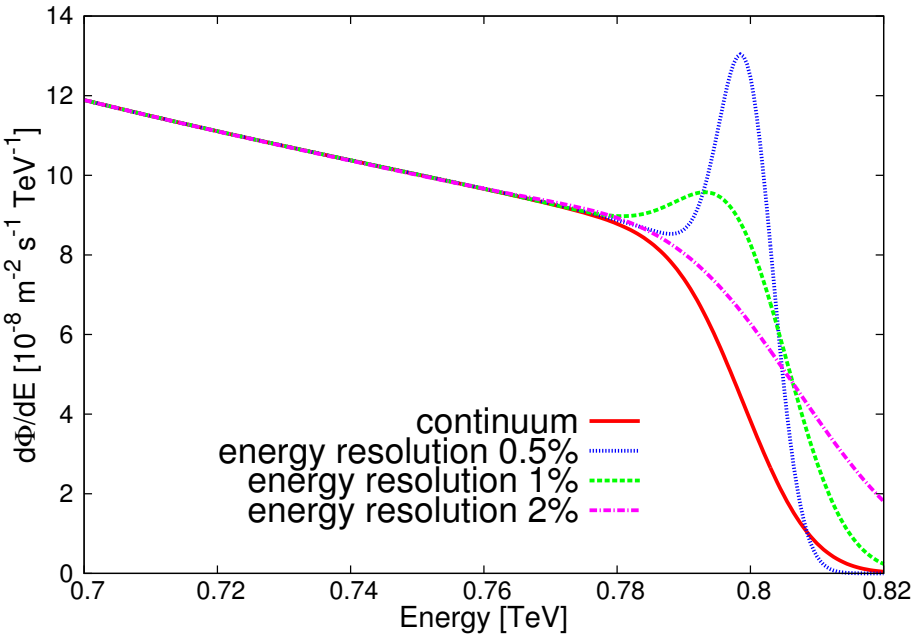

Figure 8: Gamma-ray spectra of continuum plus line diffused by the energy resolution assuming $m_{B^{(1)}} = 800$ GeV. The solid line shows the continuum component only, assuming the energy resolution of 1%, while the dotted, dashed and dot-dashed lines show the continuum plus line components assuming energy resolution values of 0.5%, 1% and 2% respectively. The assumed boost factor is 100.

error, because the shape of spectral features will be not changed. The energy resolution for gamma-ray detectors should be better than 2%, in order to "resolve the line" without the need for detailed analysis.

Now, we vary the mass from 500 GeV to 1000 GeV in 100 GeV intervals, and calculate the count spectrum for each mass. The results are shown in Fig. 11, which shows that the characteristic peak structure is visually clearer when $m_{B^{(1)}}$ is heavier. That is, the line component becomes relatively larger since the continuum component decreases for heavier $m_{B^{(1)}}$.

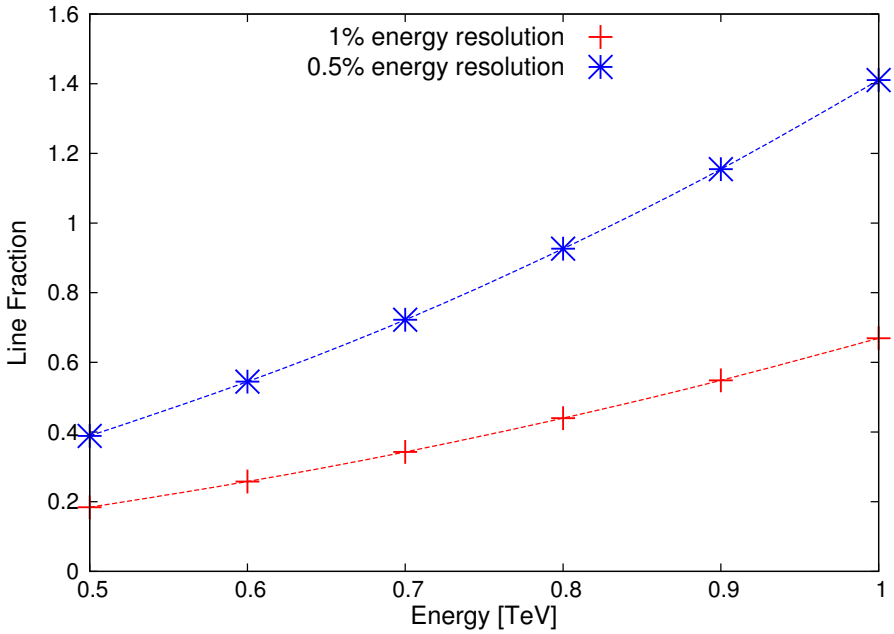

Figure 9: The line fraction as a functions of $m_{B^{(1)}}$, assuming an energy resolution of 0.5% and 1%. The dashed curve is drawn to guide to the eyes.

5.2 Constraints on the boost factor: Gamma–ray

We now discuss the observability of the LKP signal in near-future detectors, taking account of the observed background flux. That is, we give estimates for the accessible range of the boost factor when the observed counts are significantly different from the background flux. Here, we consider the gamma-ray flux from HESS J1745-290 located near the center of the Galaxy. This gamma-ray source can be identified as the Galactic center, Sgr A* [48]. Its flux above ~ 200 GeV is given by [83]

$$\frac{d\Phi}{dE} = (2.55 \pm 0.06 \pm 0.40) \left(\frac{E}{\mathrm{TeV}}\right)^{-2.10\pm0.04\pm0.10} \times \exp\left[-\frac{E}{(15.7 \pm 3.4 \pm 2.5)\mathrm{TeV}}\right] \times 10^{-8} \quad \mathrm{TeV}^{-1}\ \mathrm{m}^{-2}\ \mathrm{s}^{-1}. \tag{41}$$

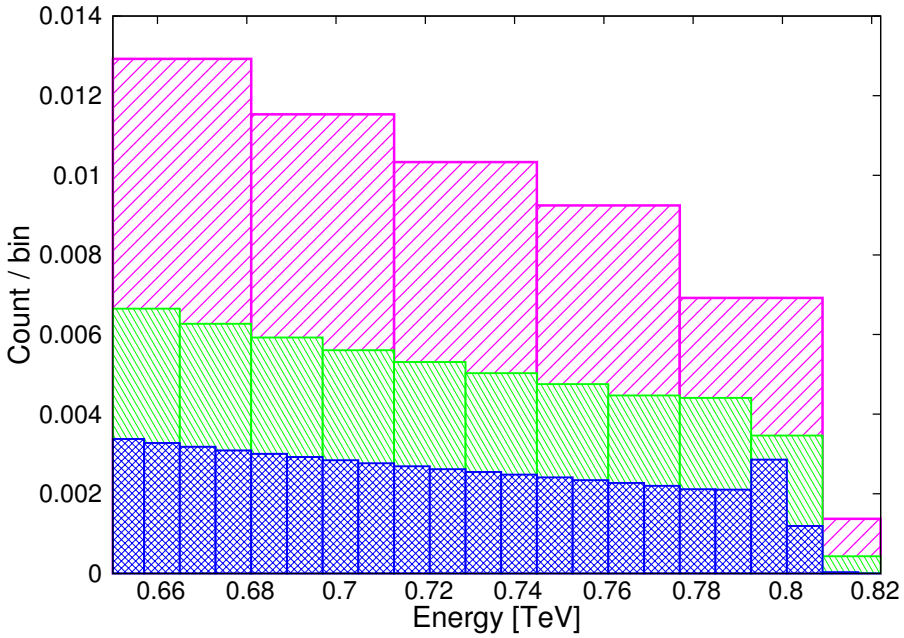

Figure 10: Expected count spectra near the peak assuming energy resolutions of 0.5%, 1% and 2% assuming $m_{B^{(1)}} = 800$ GeV and 3×10^6 m^2 s exposure. The bin widths of histograms are twice as much as 0.5%, 1% and 2% of the $m_{B^{(1)}}$, respectively. The assumed boost factor is 100.

Note that with the energy resolution of HESS (15–20%), which is a system of atmospheric Cherenkov telescopes on the ground, the LKP "line" signal is broadened and hard to detect. Compared with this point-like gamma-ray source, the diffuse Galactic gamma-ray background can be ignored in the TeV energy region thanks to the expected good angular resolution ($\sim 0.1^\circ$) of future detectors.

Now, we investigate the upper limit on the boost factor, B_f, based on the result of HESS observation. To do this, we compare a specific model with HESS data, and employ the method of χ squared test. The specific model is

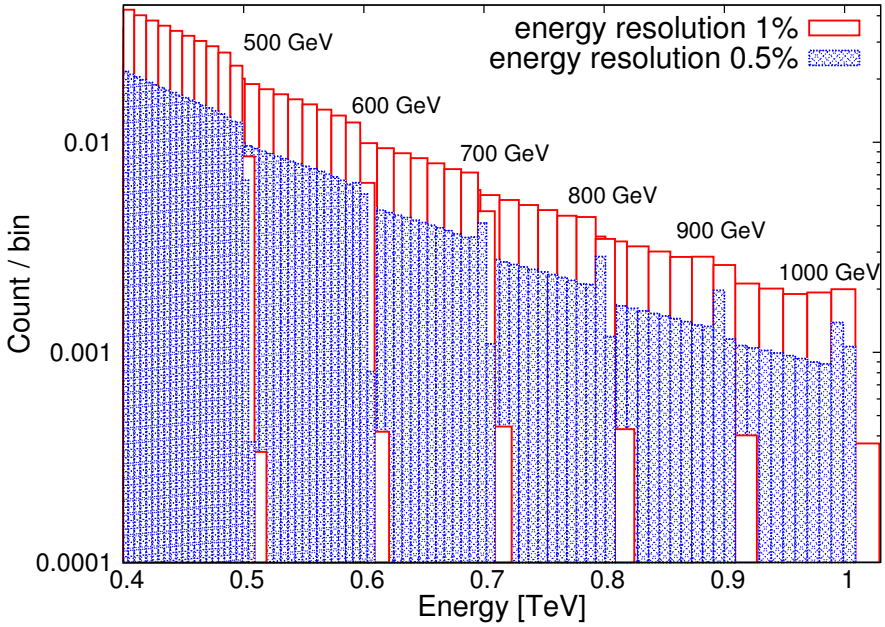

Figure 11: Expected count spectra, assuming energy resolutions of 0.5% and 1%, and 3×10^6 m^2 s exposure. The data spaces are twice as much as 0.5% and 1% of the $m_{B^{(1)}}$. The assumed boost factor is 100.

given by

$$\frac{d\Phi_\gamma}{dE_\gamma} = \frac{d\Phi_\gamma^{\rm Bkgd}}{dE_\gamma} + B_f \frac{d\Phi_\gamma^{\rm LKP}}{dE_\gamma} \tag{42}$$

$$\text{with} \quad \frac{d\Phi_\gamma^{\rm Bkgd}}{dE_\gamma} = C_B \left(\frac{E}{\rm TeV}\right)^{\Gamma_B} \exp\left[-\frac{E}{15.7\ {\rm TeV}}\right] \times 10^{-8}\ {\rm m}^{-2}\ {\rm s}^{-1}\ {\rm TeV}^{-1}$$

where C_B and Γ_B are the coefficient and index of the background flux. Here we assume that the energy resolution of detector is 20%, which corresponds to that of HESS, so the "LKP Flux", $d\Phi_\gamma^{\rm LKP}/dE_\gamma$, has the line plus continuum components blurred by 20% energy resolution.

The χ squared value is defined as

$$\chi^2 = \sum_i \frac{({\rm data}_i - {\rm model}_i)^2}{\sigma_i^2} \tag{43}$$

Table 4: The model parameter sets with maximally allowed B_f at 99% confidence level ($\chi^2 < 40.2894$).

$m_{B^{(1)}}$ [GeV]	C_B	Γ_B	B_f
500	2.30	-2.00	4
600	2.30	-2.00	7
700	2.25	-1.95	10
800	2.25	-1.95	15
900	2.25	-1.95	20
1000	2.25	-1.95	26

where "data" is the value of HESS data points, σ_i is its statistical error, and "model" is given by Eq. (42). The number of HESS data points is 25 and the number of parameters is 3 (C_B, Γ_B and B_f), so the number of degrees of freedom is 22. Thus, $\chi^2 < 40.2894$ is required to be consistent with the HESS data at 99% confidence level. We assume various values for C_B and Γ_B for the background flux, and calculate the maximum B_f under the condition as $\chi^2 < 40.2894$ for each $m_{B^{(1)}}$. The results are shown in Table 4, and we compare the model flux with HESS data assuming these parameters in Fig. 12.

Then, we consider the case for CALET observation. CALET observation was started in the second half of 2015 and the results are not publicly available. We assume some years of CALET observation, but the number of events will be limited because of the smaller satellite-size area compared with atmospheric Cherenkov telescopes. In order to investigate the detectability quantitatively, we employ the maximum likelihood method, which is suitable for small number statistics [84]. As a background, we assume the values for C_B and Γ_B given in Table 4.

The likelihood is the product of the probability of the observed count in each energy bin:

$$L = \prod_i^N p_i \tag{44}$$

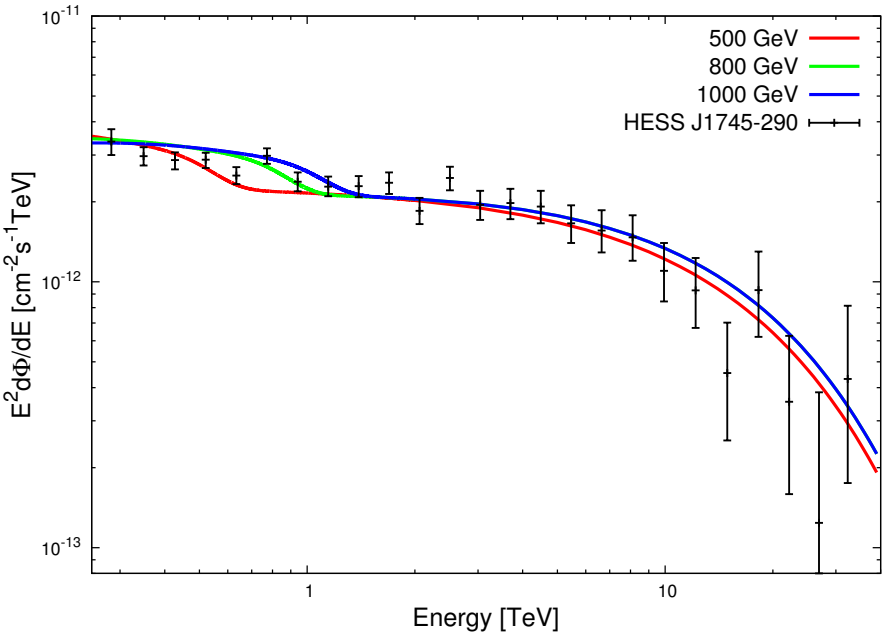

Figure 12: Comparison the LKP plus background flux assuming the model parameters given in Table 4 and 20% energy resolution with HESS observational data.

where N is numbers of energy bins, and

$$p_i = \frac{\theta_i^{n_i} e^{-\theta_i}}{n_i!} \tag{45}$$

is the Poisson probability with the observed count, n_i, and the expected count, θ_i, in the i-th energy bin predicted by a model. It is more convenient to calculate the logarithm of the likelihood:

$$\ln L = \sum_i n_i \ln(\theta_i) - \sum_i \theta_i - \sum_i \ln(n_i!). \tag{46}$$

The last term, $\sum_i \ln(n_i!)$, is model independent, and it is not useful for the likelihood ratio test, so we can ignore it. We performed Monte Carlo simulations of observations to estimate the observability of the signal quantitatively. A series of n_i is sampled from Poisson distribution whose mean is θ_i. We calculate a set of two fictitious observations: one observation assumes

θ_i of the background counts only, and the other observation assumes θ_i of the background plus signal counts. Then, we consider the test–statistic T_s derived from the likelihood ratio:

$$T_s \equiv -2(\ln L_0 - \ln L_1) \tag{47}$$

where L_0 corresponds to background counts, and L_1 corresponds to background plus signal counts. If T_s is positive, the data is better fit by the background plus signal model than by the background-only model. We generated 1000 sets of fictitious observations and obtained the distribution of T_s for each combination of model parameters ($m_{B^{(1)}}$, B_f and N). When more than 99% out of 1000 T_s's are lager than zero, we can say there is a signal in the data at 99% confidence level for those parameters.

N is related to the observed energy range which we specify as follows, for example,

$$\text{Energy range} = [10 \text{ GeV}, (m_{B^{(1)}} + 3\sigma_E) \text{ GeV}] \tag{48}$$

with the same bin width as used in Fig. 10. This lower bound of the energy range under analysis corresponds to the case of CALET observation, and the upper bound is fixed as $m_{B^{(1)}}+3\sigma_E$ to allow finite energy resolution. Hence, if we use the highest energy bin only, N equals to one. Then, we vary the lower bound of the energy range to lower energies. Thus, N gradually increases as we expand the energy range to lower energies, and the maximum number of N is about 50 and 100 for 1% and 0.5% energy resolution, respectively, for this energy range. For example, N at the peak for 0.5% energy resolution and $m_{B^{(1)}} = 800$ GeV is

$$N\left[E_{\text{peak}}, m_{B^{(1)}} + 3\sigma_E\right] = 3. \tag{49}$$

We calculate the upper limit on B_f when 99% of T_s's become larger than zero for each $m_{B^{(1)}}$ and N. The relation between N and the upper limit on B_f is shown in Fig. 13 for the case of $m_{B^{(1)}} = 800$ GeV and 1% energy resolution.

In Fig. 13, dashed and solid lines show the upper limit on B_f as a function of N in the case for 3 years observation and 10 years observation by CALET assuming $m_{B^{(1)}} = 800$ GeV and 1% energy resolution, The dotted line shows the upper limit on B_f based on HESS observational data as mentioned above. In the small N region, the limit on B_f rapidly decreases with increase N, because the contribution of the line component is significant in this region.

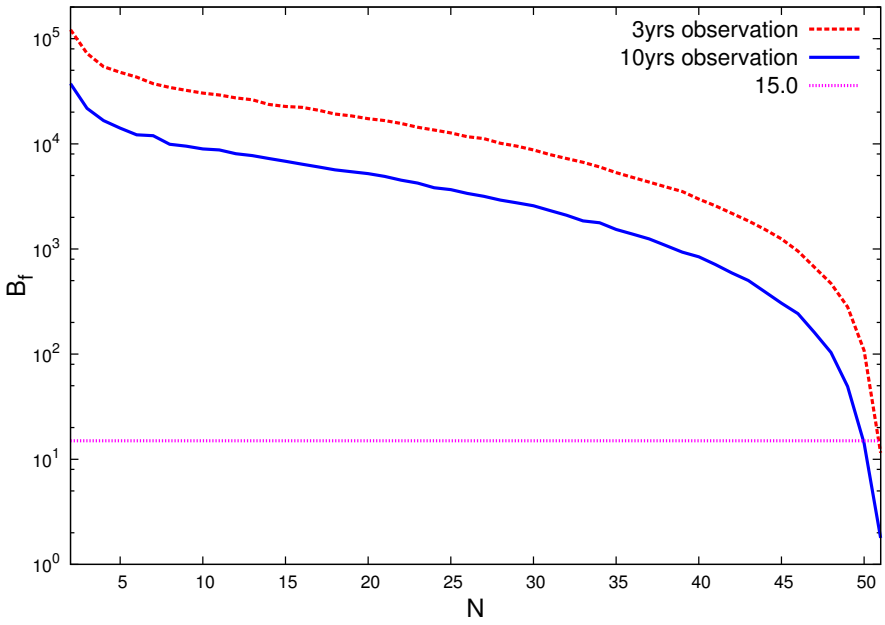

Figure 13: Expected upper limits on the boost factor B_f for the $m_{B^{(1)}} = 800$ GeV as a function of the numbers of energy bins N. The dotted line shows the upper limit obtained by χ squared test. The dashed and solid lines show the upper limits on the boost factor (99% C.L.) for energy resolution 1% and $m_{B^{(1)}} = 800$ GeV, assuming 3 years and 10 years observation of CALET.

From Fig. 13, by assuming $m_{B^{(1)}} = 800$ GeV, 1% energy resolution and 10 years observation by CALET, we can set more strict constraint on B_f than HESS observation, if we utilize the whole energy region.

We apply similar analyses for other LKP masses, and the results are summarized in Fig. 14 calculated for energy resolution of 1% and 0.5%. This figure indicates that the constraint for B_f could be tighter for lighter $m_{B^{(1)}}$. For a large N, or wide–band observation, the constraint on B_f would be as small as about 2. This is because the quark fragmentation contribution included in continuum emission increases in the lower energy region and the expected energy spectrum deviates from a single power–law. Thus, wide–band observation has an advantage just to constrain B_f, but lacks distinctive spectrum feature ("line") for identification.

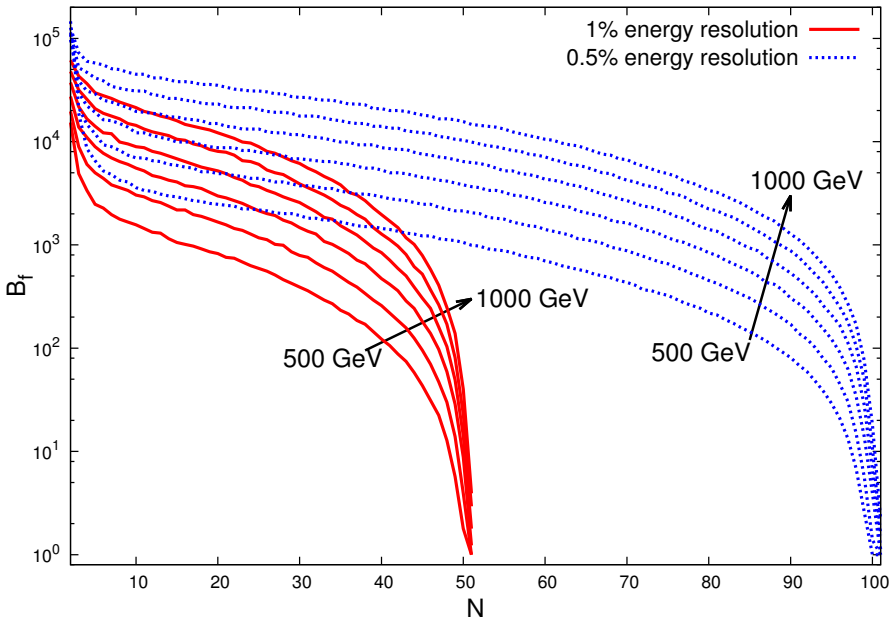

Figure 14: Comparison of the expected upper limits on the boost factor B_f (99% C.L.) with 1% and 0.5% energy resolution. The individual lines refer to the cases with $m_{B^{(1)}}$ varied from 500 GeV to 1000 GeV in 100 GeV intervals.

6 The electron and positron signal

In 2002, Cheng *et al.* [85] predicted that the electron plus positron spectrum from annihilation of LKP would show a characteristic edge structure near the LKP mass. The edge structure was calculated by Moiseev *et al.* [86] for Fermi–LAT detection, but, at least in the energy range below 300 GeV, such structure has not established so far (see, e.g. Ref. [56]). On the other hand, above 300 GeV, the observational data are still limited, so the characteristic structure could be observed in near–future missions. For example, CALET started exploring the energy range up to 20 TeV for electrons and positrons [87].

When LKP pairs annihilate, there are some modes which produce electrons and positrons as final products, and we categorize them into two components. One of them is a "line" component, which consists of electron–positron pairs directly produced by annihilation, and gives rise to edge structure near the LKP mass after propagating in the Galactic halo to Earth. Another is a "continuum" component, which consists of secondarily produced electrons and positrons via muon pairs, tauon pairs, quark pairs, and gauge bosons produced by LKP annihilation. We use the spectra for line and continuum components given by Cirelli *et al.* [88] and Ciafaloni *et al.* [89], which are shown in Fig. 15, where the solid line indicates the line spectrum and patterned lines show the continuum spectra from muon pairs, tauon pairs, quark pairs (b, t, c), and gauge bosons, respectively. Note that the line spectra shows a tail toward lower energies due to final state interactions. For comparison, the positron spectra without electroweak corrections are shown in thin lines for the line spectrum and the continuum spectrum for muon pairs. One can see the electroweak correction affects the spectra in the lower energy region [88, 89].

The spectra for line and continuum components shown in Fig. 15 are those just after pair annihilation, and we have to take account of the effects of propagation in the Galactic halo to Earth, such as diffusion and energy loss processes. For this purpose, we follow the Green function approach given by Moskalenko and Strong [90], assuming the "Isothermal model" as the halo profile for reference.

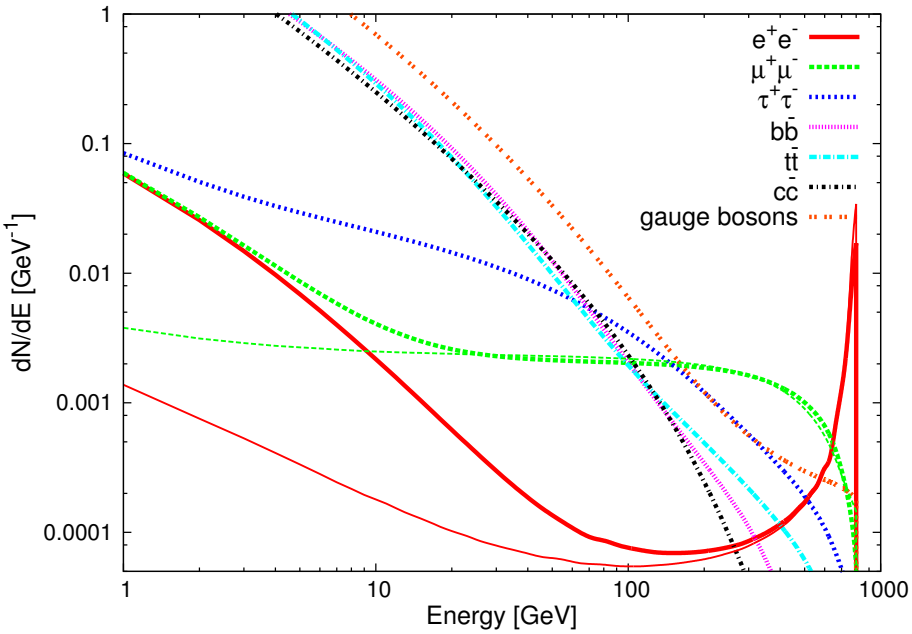

Figure 15: The "continuum" and "line" positron spectra from LKP annihilations for $m_{B^{(1)}} = 800$ GeV [88, 89]. The patterned lines correspond to the positron spectrum per annihilation via muon pairs, tauon pairs, quark pairs, and gauge bosons, respectively. The solid line corresponds to the line component. The thick lines include the electroweak corrections, and the thin lines do not include those corrections.

6.1 The effect of propagation

Charged particles, such as electrons and positrons, produced by LKP annihilation around the center of the Galaxy change their direction randomly by the irregular component in the Galactic magnetic field, and lose their energies. Thus, the observational electron plus positron fluxes have different shapes from initial ones. We consider the effective elements for propagation in the following section.

6.1.1 The energy loss function for electron and positron in the Galaxy

We review the calculation for the energy loss function here, and more detailed discussions are given in Refs. [91, 92], for example.

We consider the effects of the energy losses of electrons and positrons during their propagation in the Galaxy caused by Coulomb interactions with the interstellar (IS) matter, by ionization processes with the IS matter, by bremsstrahlung in the IS matter, by inverse Compton scattering (ICS) and by synchrotron emission. Thus, the total energy loss rate can be written as sum of these components;

$$-\frac{dE}{dt} = \left(-\frac{dE}{dt}\right)_{\rm Coul+Ioniz} + \left(-\frac{dE}{dt}\right)_{\rm Brems} + \left(-\frac{dE}{dt}\right)_{\rm ICS} + \left(-\frac{dE}{dt}\right)_{\rm Sync} \quad (50)$$

where E is the energy of electron or positron. In the following, we will briefly give expression for these energy loss functions.

(i) *Coulomb interactions and Ionization processes*

On neutral matter, the energy loss rate is described by

$$\left(-\frac{dE}{dt}\right)_{\rm Neut} = \frac{9}{4} c\,\sigma_T\,m_e \sum_i n_i\,Z_i \left(\log\frac{E}{m_e} + \frac{2}{3}\log\frac{m_e}{\Delta E_i}\right) \quad (51)$$

where c is the speed of light, $\sigma_T = 8\pi r_e^2/3$ with $r_e = \alpha/m_e$, ($\alpha \sim 1/137$ is a fine structure constant) is the Thomson cross section, Z_i is the atomic number of the matter or gas species i, n_i is the number density for them, and ΔE_i is the average excitation energy.

On the other hand, the energy loss rate for ionized matter is given as

$$\left(-\frac{dE}{dt}\right)_{\rm Ioniz} = \frac{3}{4} c\,\sigma_T\,m_e\,n_e \left(\log\frac{E}{m_e} + 2\log\frac{m_e}{E_{\rm Pla}}\right) \quad (52)$$

where n_e is the electron number density and $E_{\rm Pla}$ is the characteristic energy of the plasma.

The total energy losses for Coulomb interactions and ionized processes is given by sum of Eq. (51) and Eq. (52). These energy loss rates do not essentially depend on E, because the constant terms will be numerically dominant in the brackets.

(ii) *Bremsstrahlung*

The energy loss rate for bremsstrahlung is described by

$$\left(-\frac{dE}{dt}\right)_{\rm Brems} = c\sum_i n_i(r,z)\int_0^E dE_\gamma\, E_\gamma \frac{d\sigma_i}{dE_\gamma} \tag{53}$$

where r and z are cylindrical galactic coordinates, and E_γ is the energy of the gamma–ray emitted in each bremsstrahlung process. The differential cross section is given as

$$\frac{d\sigma_i(E,E_\gamma)}{dE_\gamma} = \frac{3\alpha\sigma_T}{8\pi E_\gamma}\left\{\left[1+\left(1-\frac{E_\gamma}{E}\right)^2\right]\phi_1^i - \frac{2}{3}\left(1-\frac{E_\gamma}{E}\right)\phi_2^i\right\} \tag{54}$$

where ϕ_1^i and ϕ_2^i are scattering functions dependent on the properties of the scattering system. The energy loss rate caused by bremsstrahlung depends on E linearly at leading order. More details are discussed in Ref. [91], for example.

(iii) *Inverse Compton Scattering (ICS)*

For ICS, the energy loss rate is written as

$$\begin{aligned}\left(-\frac{dE}{dt}\right)_{\rm ICS} = 3c\sigma_T\int_0^\infty d\epsilon\,\epsilon\int_{1/4\gamma^2}^1 dq\, n(\epsilon,r,z)\frac{(4\gamma^2-\Gamma_\epsilon)q-1}{(1+\Gamma_\epsilon q)^2} \\ \times\left[2q\ln q + q + 1 - 2q^2 + \frac{1}{2}\frac{(\Gamma_\epsilon q)^2}{1+\Gamma_\epsilon q}(1-q)\right]\end{aligned} \tag{55}$$

where $n(\epsilon,r,z)$ is the number density per unit volume and unit energy of photons of the interstellar radiation field with energy ϵ, $\gamma = E/m_e$ is the relativistic factor of the electrons and positrons, and $\Gamma_\epsilon = 4\epsilon\gamma/m_e$.

For low electron energies, that is in the Thomson limit, the energy loss rate is expressed as

$$\left(-\frac{dE}{dt}\right)_{\rm ICS} = \frac{4c\sigma_T}{3m_e^2}E^2\int_0^\infty d\epsilon\, n(\epsilon,r,z) \tag{56}$$

so the energy loss rate for ICS is proportional to E^2 for low energy region.

(iv) *Synchrotron emission*

For synchrotron emission, the energy loss rate is written as

$$\left(-\frac{dE}{dt}\right)_{\rm Sync} = \frac{4c\sigma_T}{3m_e^2}E^2\frac{B^2}{8\pi} \tag{57}$$

where B is the strength of the magnetic field. The energy loss rate for synchrotron emission is also proportional to E^2.

These are the energy loss rates for electrons and positrons during their propagation in the Galaxy.

6.1.2 The effect of propagation in the concrete case

The effects of propagation are studied by Moskalenko and Strong [90], and we calculate the modulated flux by using their results given as parameterized Green functions.

The positron flux is given by [90];

$$\frac{d\Phi_{e^+}}{d\Omega dE} = \langle\sigma v\rangle B_f \left(\frac{\rho_0}{m_{B^{(1)}}}\right)^2 \sum_i B_i \int d\epsilon \frac{dN_i}{d\epsilon} g\left(\epsilon, E\right) \ \mathrm{cm}^{-2}\mathrm{s}^{-1}\mathrm{sr}^{-1}\mathrm{GeV}^{-1} \tag{58}$$

where B_i is a branching ratio for each particle, and ρ_0 is the local dark matter density. The annihilation cross section, $\langle\sigma v\rangle$, to yield the significant relic density of cold dark matter is the order of 3×10^{-26} cm^{3}s^{-1} [12] (see also Section 2).

The Green function, $g(\epsilon, E)$, is defined as

$$g\left(\epsilon, E\right) = \frac{10^{25}}{E^2} 10^{a(\log_{10} E)^2 + b(\log_{10} E) + c}\, \theta\left(\epsilon - E\right) \tag{59}$$

where E is the observed energy in GeV and the parameters a, b and c are tabulated in Ref. [90], which gives the spectra of electron and positron after propagation, for monochromatic energy (ϵ) injection. Figure 16 shows the calculated Green function in units of 10^{25} GeV cm sr^{-1} for "Isothermal" halo model given in Ref. [90]. Here, we assume the halo size $z = 8.5$ kpc and several injection energies $\epsilon = 25$, 50, 100, 200, 400 and 800 GeV.

In addition, we should take account of the effects of solar modulation in the low energy region below 10 GeV. The magnetic field of the Sun is the source of the observed modulation of the Galactic cosmic rays. Solar

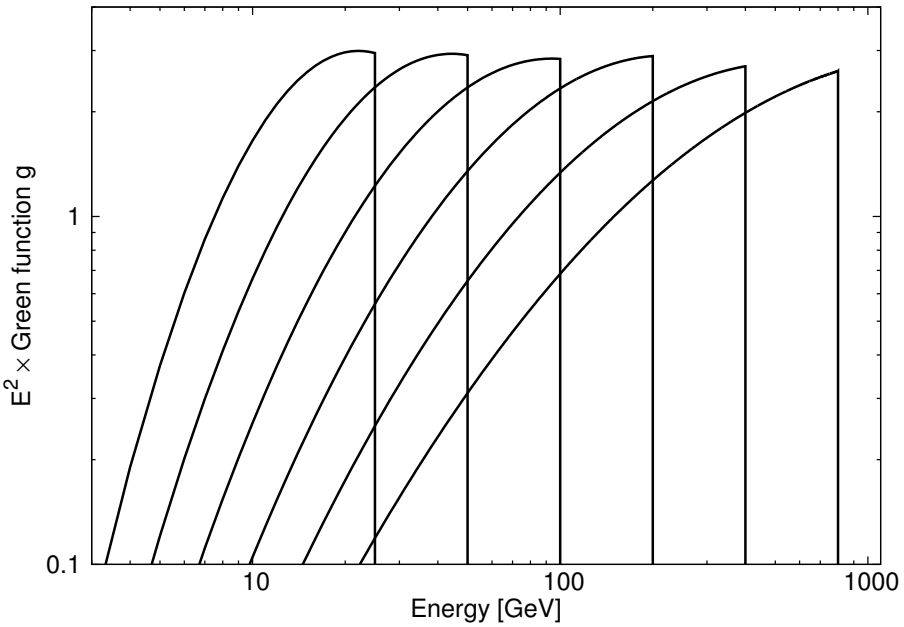

Figure 16: Calculated Green function in units of 10^{25} GeV cm sr^{-1} for "Isothermal" halo model [90], assuming halo size $z = 8.5$ kpc and injection energies $\epsilon = 25$, 50, 100, 200, 400 and 800 GeV.

modulation is dominant on low energy particles, and affects on spectral shape for cosmic rays. In the force field approximation, the differential flux of particles of mass m and charge Ze, $\Phi(E)$, reaching Earth with energy E is related to the interstellar flux, $\Phi(E_{IS})$, as

$$\Phi(E) = \frac{E^2 - m^2}{E_{IS}^2 - m^2}\Phi(E_{IS}) \tag{60}$$

where E_{IS} is the energy in interstellar space and related to E as $E = E_{IS} - |Z|\phi$, and ϕ is a solar modulation potential [93].

The line component is approximately in the form of δ–function before propagation in the Galactic halo. However, its spectrum after propagation in the Galactic halo to Earth extends to lower energies caused by the effects of diffusion and energy loss processes. In addition to the line component, we also calculate the continuum component. The continuum component has a broad spectrum extending to lower energies when it is produced by LKP

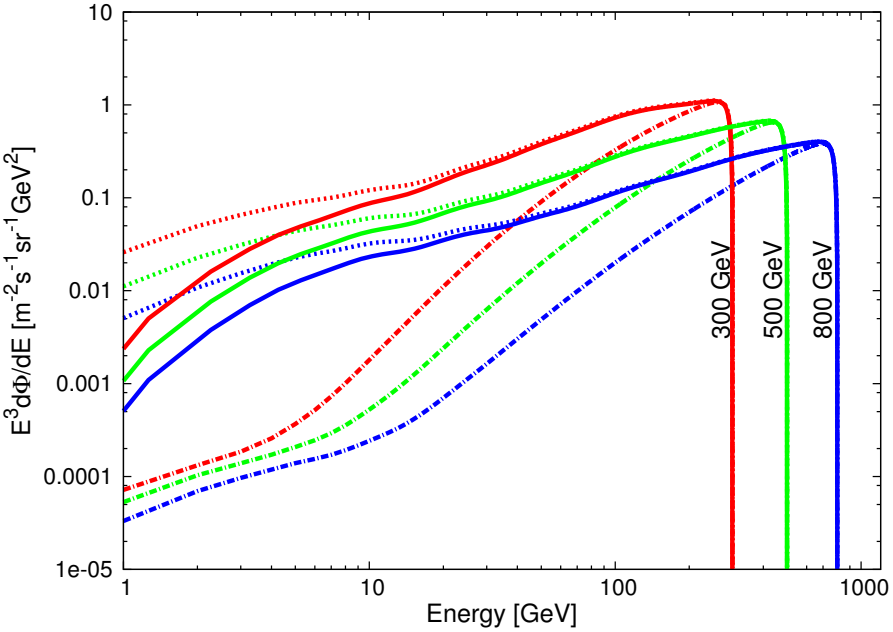

Figure 17: The fluxes of electrons plus positrons from LKP annihilation after propagation for three assumed LKP masses. The dot–dashed lines show the flux without solar modulation for "line" component only, the dotted lines show the total flux from LKP annihilation ("continuum" plus "line") without solar modulation, and the solid lines show the total flux including effect of solar modulation with the solar modulation potential $\phi = 735$ MV. We assume the boost factor $B_f = 1$.

annihilation as shown in Fig. 15. Then we calculated the spectrum after propagation using the Green function similarly to the case of the line component. These results are shown in Fig. 17, where the dot–dashed lines show the flux for the line component only without solar modulation, the dotted lines show the total flux from LKP annihilation (continuum plus line) without solar modulation, and solid lines show the total flux including effect of solar modulation assuming a solar modulation potential $\phi = 735$ MV [94] for three assumed LKP masses. This figure indicates the continuum component becomes dominant in lower energies, and it is larger by two orders of magnitude around 10 GeV than the line component. We checked our calculation by comparing with a similar calculation given by Boudard *et al.* [95],

and learned that the two calculations give essentially the same result; small differences could be caused by different assumptions made in calculations.

6.2 Constraints on the boost factor: Electron and Positron

Now, we compare the electron plus positron fluxes derived from LKP annihilation with recent measurements, and discuss possible constraints on the boost factor. Figure 18 shows the positron fraction given by recent measurements [56, 57, 96] with a prediction by the cosmic–ray secondary (hereafter "conventional") electron and positron calculation by Yuan and Bi [94]. We derive the LKP flux, $F_{\rm LKP}$, which fits the measured positron fraction assuming the conventional electron plus positron fluxes in the differential form, $F_{\rm Conv}$, as given in Ref. [94]. The LKP pair annihilation creates the same number of electrons and positrons, so the positron fraction for the LKP flux, $f_{\rm LKP}$, always equals to 0.5. On the other hand, the positron fraction for the conventional fluxes, $f_{\rm Conv}$, is smaller than 0.1, depending on energy [94]. Then, the total positron fraction is given by

$$\text{Positron Fraction} = \frac{F_{\rm LKP} \times B_f \times f_{\rm LKP} + F_{\rm Conv} \times f_{\rm Conv}}{F_{\rm LKP} \times B_f + F_{\rm Conv}}, \tag{61}$$

where B_f is the boost factor. With this prescription, we calculate the positron fractions for several assumed LKP masses as a function of energy to fit the AMS–02 data [57] at 100 GeV as shown in Fig. 18. One can see the observed data can be fit by adding the LKP flux well, but the fit becomes worse if we do not include the continuum component.

The values of the boost factor derived as above for each LKP mass are plotted in Fig. 19. Here, we show the boost factors for three halo models ("Isothermal", "Evans", "Alternative"). The dark matter mass densities for each model are given as [90]:

$$\begin{aligned}
\rho(r) &= \rho_0 \frac{r_c^2 + R_\odot^2}{r_c^2 + r^2} \qquad \text{for Isothermal halo model} \\
\rho(r) &= \rho_0 \frac{(r_c^2 + R_\odot^2)^2}{3r_c^2 + R_\odot^2} \frac{3r_c^2 + r^2}{(r_c^2 + r^2)^2} \qquad \text{for Evans halo model} \\
\rho(r) &= \rho_0 \frac{(r_c + R_\odot)^2}{(r_c + r)^2} \qquad \text{for Alternative halo model}
\end{aligned} \tag{62}$$

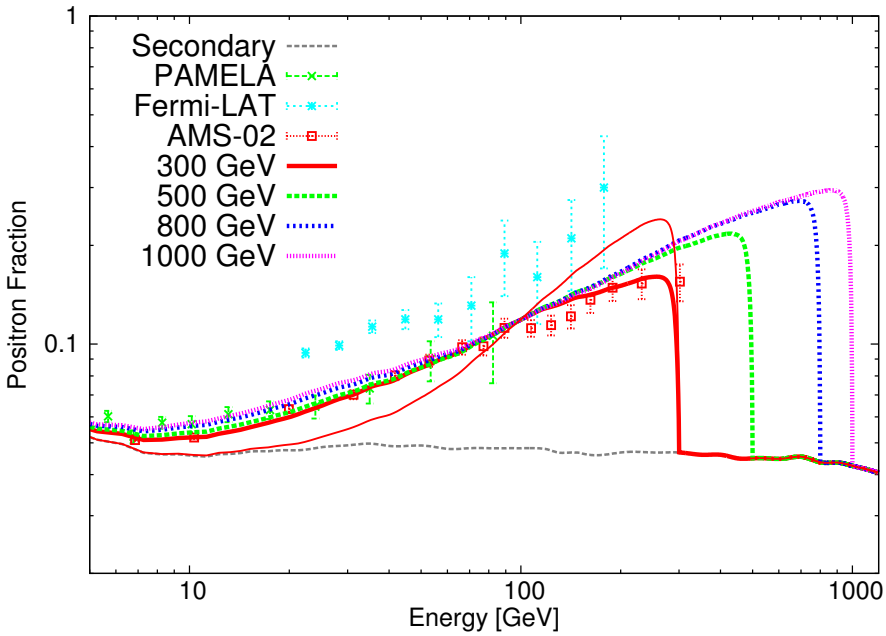

Figure 18: The positron fraction expected from LKP annihilation (thick lines) compared with recent measurements [56, 57, 96], and a prediction by the cosmic–ray secondary electron and positron calculation (thin dashed line) [94]. Thin solid line shows the expected fraction without the continuum component for $m_{B^{(1)}} = 300$ GeV.

where ρ_0 is the local dark matter density for each model, r_c is the core radius, $R_\odot = 8.5$ kpc is the distance from the Galactic center to the solar system, and r is the spherical coordinate. We plot these profiles in Fig. 20, and also show the Green functions for each model in Fig. 21, which indicates that while the Green functions for these models are similar behavior in the high energy region, the "Alternative" model seems to give rather larger values than other models in the lower energy region.

The values for these parameters, such as ρ_0 and r_c, which are fitted to the rotation curve, are given in Ref. [90]. For these three models the boost factor shows a similar behavior as is shown in Fig. 19, and small differences indicate a typical systematic error in estimating the boost factor.

With the derived boost factors from the positron fraction, we compare the expected electron plus positron spectra, $E^3 \times (F_{\rm LKP} \times B_f + F_{\rm Conv})$, with

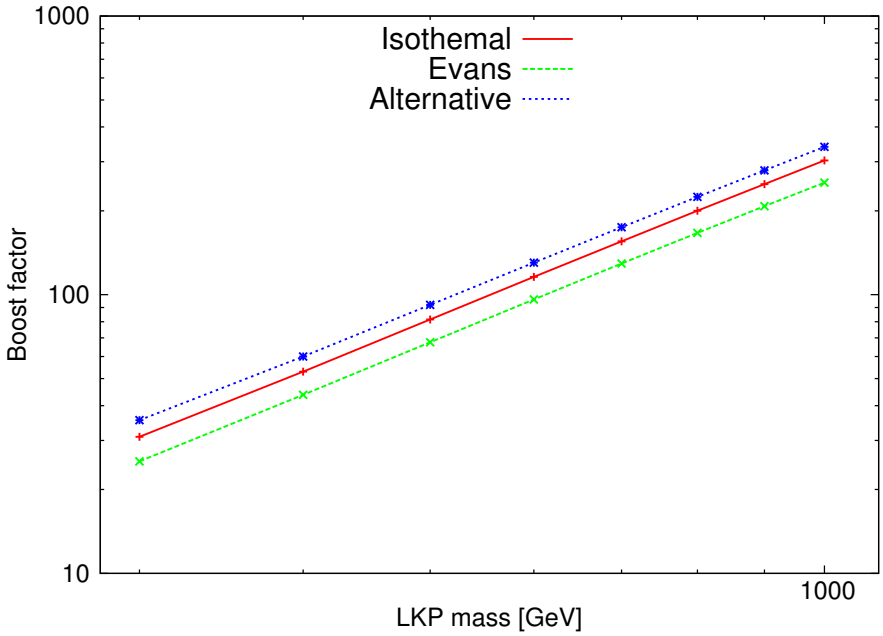

Figure 19: The boost factor derived from the positron fraction fit to the AMS–02 data at 100 GeV as a function of the assumed LKP mass for three halo models. The solid, dashed, and dotted lines show the boost factor for "Isothermal", "Evans", "Alternative" halo model, respectively. Here we assume $\langle \sigma v \rangle = 3 \times 10^{-26}$ cm^{3}s^{-1}.

recent observational data as shown in Fig. 22. It indicates that light LKP, such as $m_{B^{(1)}} = 300$ GeV, is not compatible with measurements as the dominant component of the Galactic halo dark matter, since the characteristic edge–like structure expected around 300 GeV seems to be incompatible with the measurements. However, heavy LKP, such as $m_{B^{(1)}} = 1000$ GeV, could not be excluded, because in the energy region around 1000 GeV, the measurements suffer rather large statistical uncertainties. Thus, we hope near–future missions with better sensitivity will clarify the existence (or non–existence) of the LKP dark matter.

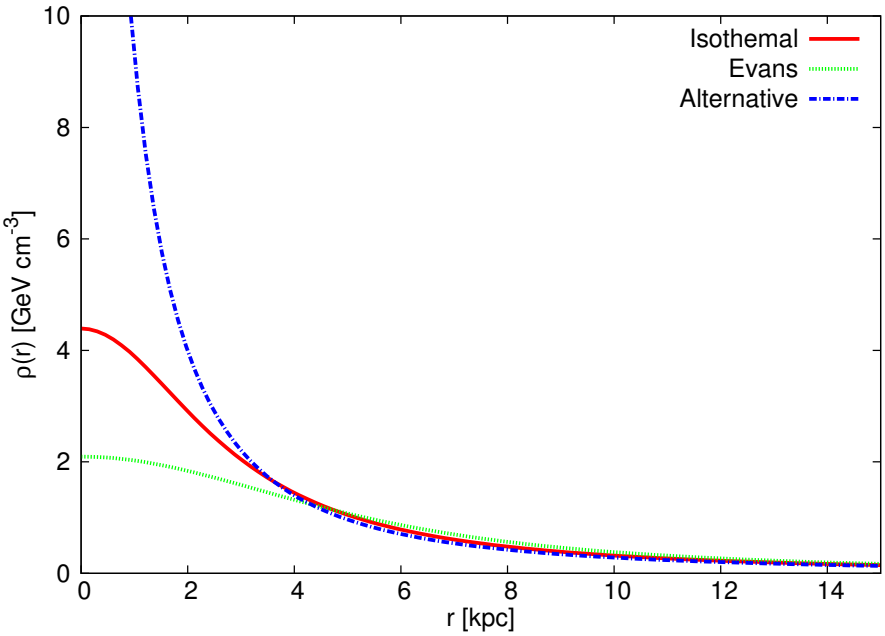

Figure 20: The dark matter mass density profiles for three halo models. The solid, dotted and dot-dashed lines show that for "Isothermal", "Evans" and "Alternative" halo model [90], respectively.

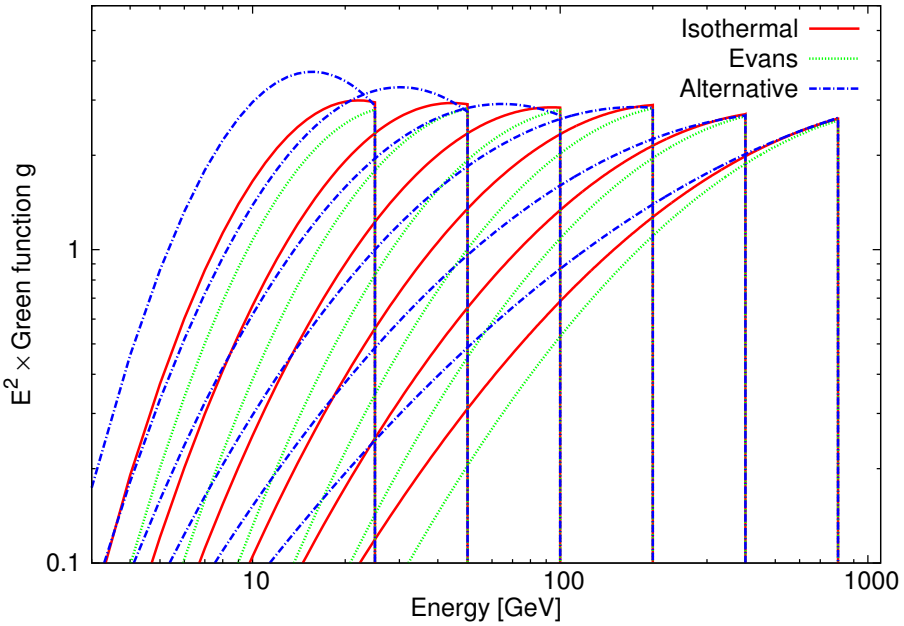

Figure 21: Calculated Green function in units of 10^{25} GeV cm sr^{-1} for three halo models, assuming halo size $z = 8.5$ kpc and injection energies $\epsilon = 25$, 50, 100, 200, 400 and 800 GeV. The solid, dotted and dot-dashed lines show that for "Isothermal", "Evans" and "Alternative" halo model [90], respectively.

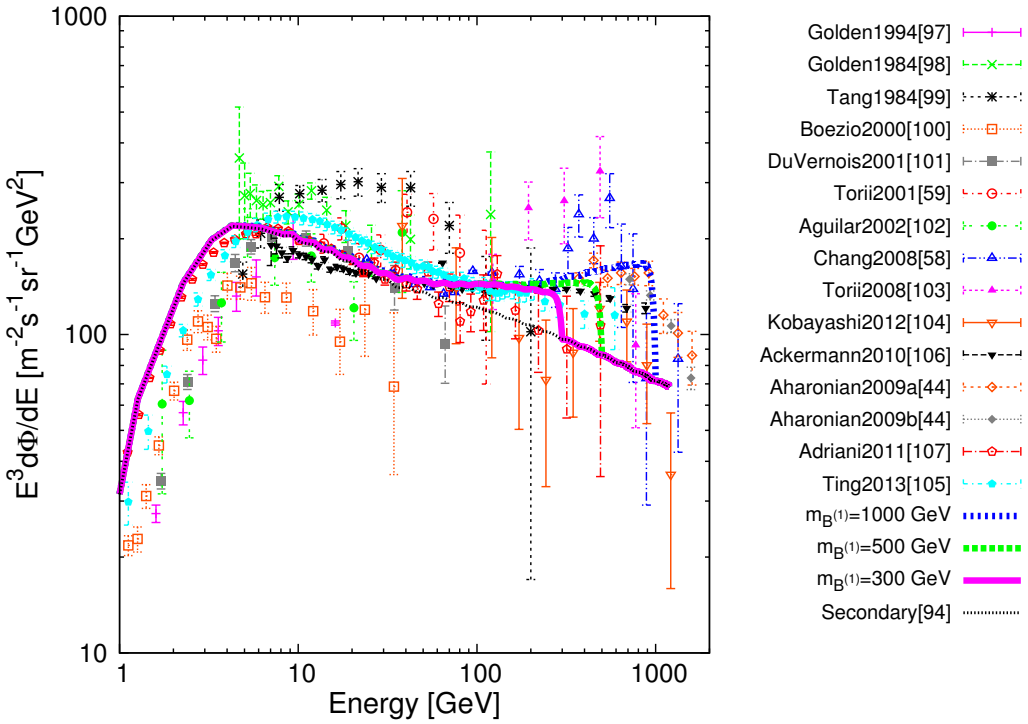

Figure 22: The electron plus positron spectra assuming several LKP masses and boost factors to fit the AMS–02 data at 100 GeV (thick lines) compared with recent observational data [44, 58, 59, 97, 98, 99, 100, 101, 102, 103, 104, 105, 106, 107], and a prediction by the cosmic–ray secondary calculation (thin dotted line) [94].

7 Discussion

Now, we discuss the results from gamma–ray signal and electron plus positron signal in relation to the boost factor.

First, we consider the range of parameters, which are LKP mass $m_{B^{(1)}}$, boost factor B_f and energy bins N. The accessible range for the upper limits on the boost factor from the gamma-ray analysis is about in range from 2 to 2×10^5 as is shown in Fig. 14, where the smallest limit 2 corresponds to the case for N taking the whole energy region into account, and the largest limit 2×10^5 corresponds to the case for $N = 2$. On the other hand, in the case for electron and positron analysis, the boost factor is obtained in the range from about 30 to 300 to fit the positron fraction to AMS-02 observational data, depending on $m_{B^{(1)}}$, from 300 GeV to 1000 GeV. Hereafter, we consider the LKP mass should be in the range from 500 GeV to 1000 GeV, because light LKP mass, such as $m_{B^{(1)}} = 300$ GeV, may be excluded by recent measurements as discussed in Section 6.2.

Table 5, 6 and 7 show the parameters assuming "Isothermal", "Evans" and "Alternative" halo model, respectively. Here, parameters are LKP mass $m_{B^{(1)}}$, boost factor B_f to fit the positron fraction data given by AMS-02, and a number of energy bins, N, assuming 1% (0.5%) energy resolution and 10 years observation. This N corresponds to the minimum energy bandwidth to detect the LKP signal significantly for each $m_{B^{(1)}}$ and corresponding B_f derived from positron fraction. Among the three halo models, the "Evans" halo model gives the minimum boost factor. Although the differences indicate systematic errors in our calculation, they are in the order of several to $\sim 20\%$ and do not affect our conclusion significantly.

If we assume $m_{B^{(1)}}$ equals to 500 GeV with assuming "Isothermal" halo model, the boost factor would be 81 to fit the positron fraction. This value corresponds to $N \geq 43$ for 1% energy resolution and $N \geq 90$ for 0.5% energy resolution to affect gamma-ray spectrum. In the other words, if we observe gamma rays with wider energy bandwidth than the corresponding number of energy bins N, the LKP signal could be statistically significant.

The detectability of gamma–rays from dark matter annihilation has been discussed in literatures. Bergström *et al.* [108] discussed the relation between the mass of dark matter and cross section, and gave an upper limit for the cross section by using experimental data. In our calculation, for $m_{B^{(1)}} = 800$ GeV, 0.5% energy resolution and 10 years observation around the peak ($N = 5$), the upper limit on B_f is about 3×10^4, and if we take the whole

Table 5: The boost factor required to fit the positron fraction and the minimum number of energy bins to obtain gamma-ray signal for each LKP mass, assuming "Isothermal" halo model.

$m_{B^{(1)}}$ [GeV]	The fitted value of B_f by $e^{\pm}$	Number of Energy Bins N
500	81	43 (90)
600	116	45 (93)
700	155	46 (94)
800	200	47 (96)
900	250	48 (97)
1000	300	48 (97)

energy region, the constraint on B_f is about 2. On the other hand, the result of Ref. [108] indicates the upper limit on the cross section is about 7×10^{-28} cm^3 s^{-1} assuming 800 GeV dark matter mass for HESS–II observation. Assuming 130 pb for the cross section for annihilation into photon pairs, this upper limit corresponds to about $B_f = 180$. In our calculation, $B_f = 180$ ($m_{B^{(1)}} = 800$ GeV and 0.5% energy resolution) corresponds to about $N = 96$ and energy bandwidth of 760 GeV. Thus, if we analyze the obtained data taking account of whole energy region, these constraints can be regarded as comparable. Therefore, the limit on B_f or the cross section by Bergström *et al.* [108] may not be inconsistent with our result.

The upper limit on B_f for gamma-ray signal is given by the observational data around the Galactic center. On the other hand, the calculation for the value of B_f to fit the positron fraction is obtained by the observation of electrons and positrons, which are produced by annihilation of LKP far from the Galactic center, in the order of several kpc. Thus, perhaps we should not simply compare the limit on B_f obtained by analysis of gamma-ray flux with the value of B_f to fit the positron fraction. Nevertheless, we should note that the upper limits on B_f given by the analysis of HESS observational data, which are given in Table 4, have smaller value than the limit derived from the positron fraction fit to the AMS–02 data at 100 GeV. As shown in Table 4, the range of limits is from 4 to 26, so the values for B_f obtained by fitting to the positron excess might be already excluded by the gamma-ray observation of HESS.

Table 6: The boost factor required to fit the positron fraction and the minimum number of energy bins to obtain gamma-ray signal for each LKP mass, assuming "Evans" halo model.

$m_{B^{(1)}}$ [GeV]	The fitted value of B_f by $e^{\pm}$	Number of Energy Bins N
500	68	44 (92)
600	96	45 (94)
700	130	47 (95)
800	166	47 (97)
900	207	48 (97)
1000	252	48 (98)

On the other hand, by CALET observation, we can set more strict constraints on B_f, if we analyze the observational data taking account of whole energy region, as mentioned in Section 5.2. In addition, when we can observe enough gamma-ray events with 0.5% energy resolution detector, and we use the parameters set given in Table 4, we can plot the flux as is shown in Fig. 23. In this figure, the solid lines show the flux assuming observed with 0.5% energy resolution, and other lines and points are the same as Fig. 12. Thus, if we detect large number of gamma-ray events in near-future missions, we can expect that the characteristic peak structure appears around the LKP mass energy region.

In this paper, we point out that CALET, which is smaller in effective area but has better energy resolution compared with those of HESS-II, has a chance to detect the "line" component, not just setting an upper limit on the boost factor. Bringmann *et al*. [109] discuss the detectability for generic models and treat the line and continuum component separately, assuming observation by atmospheric Cherenkov telescopes with 10% energy resolution. Here, we consider the specified model, which is the annihilation of LKP dark matter and includes the line and continuum component mixed at the predicted fraction, assuming high–energy–resolution detectors.

Table 7: The boost factor required to fit the positron fraction and the minimum number of energy bins to obtain gamma-ray signal for each LKP mass, assuming "Alternative" halo model.

$m_{B^{(1)}}$ [GeV]	The fitted value of B_f by $e^{\pm}$	Number of Energy Bins N
500	92	42 (89)
600	130	44 (92)
700	175	46 (94)
800	225	47 (95)
900	280	47 (96)
1000	340	48 (97)

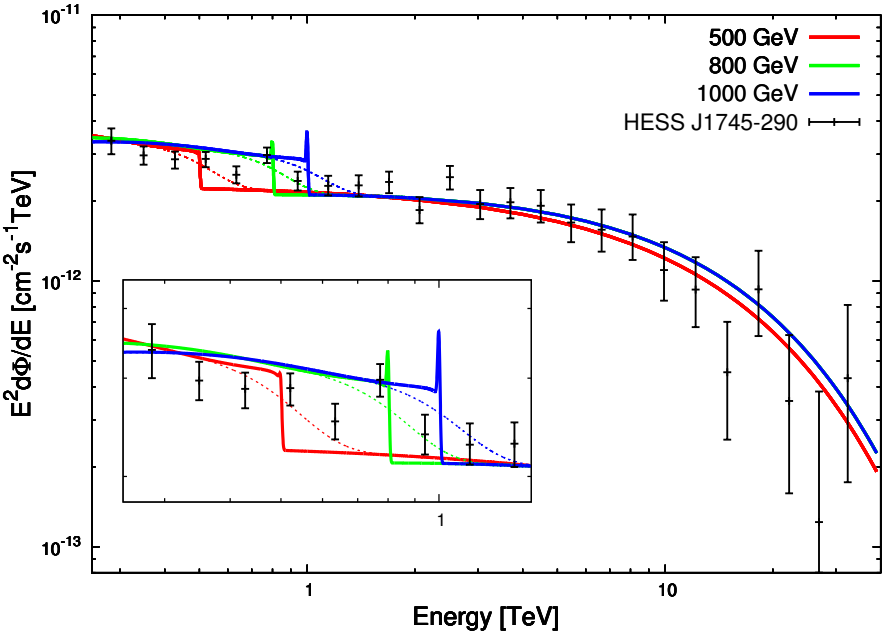

Figure 23: Comparison the LKP plus background flux with HESS data. The solid lines show the flux assuming observed with 0.5% energy resolution, and other lines and points are the same as Fig. 12.

8 Conclusion

In this paper, we discussed the observability of characteristic spectral feature appearing in secondarily produced gamma rays, electrons and positrons from annihilation of LKP dark matter near the Galactic center. Here, we conclude the results from these analyses and discussions.

Energy resolution plays a key role in detecting the line structure of the gamma-ray spectral features expected from annihilation of LKP dark matter as predicted by UED theories. This paper investigated the effects of energy resolution of gamma-ray detector and calculated the expected count spectrum. The predicted gamma-ray spectrum is the sum of the continuum and a line corresponding to the LKP mass, $m_{B^{(1)}}$, but this characteristic structure is diluted when we take account of the finite energy resolution of detectors as shown in Fig. 7 and Fig. 8. Further, if we assume the exposure (area multiplied by observation time) of near-future detectors, count statistics will be the final limiting factor as per Fig. 10. The characteristic peak indicating $m_{B^{(1)}}$ would be diffused if the energy resolution is 2% or worse. However, with quantitative statistical analysis, we may be able to detect a peak statistically by subtracting a background from the observed spectrum. In addition, if $m_{B^{(1)}}$ is heavy, the observed gamma-ray spectrum will show the characteristic peak clearly because the continuum component decreases relative to the line component, as is shown in Fig. 9.

We also investigated the electron and positron spectra from LKP annihilation taking account of propagation effects in the Galaxy. We paid particular attention to the calculation of the "continuum" emission, which is a secondary product of LKP annihilation, in addition to the "line" component directly produced by annihilation. The result shown in Fig. 17 indicates the "continuum" component dominates over the "line" component in the low energy region after propagation in the Galactic halo to Earth, and changes the shape of the positron fraction, as shown in Fig. 18

We estimated the value of the boost factor by using the positron fraction measurement by AMS–02. The result implies the boost factor should be in the range from about 30 to 300, depending on the LKP mass in the range of 300 to 1000 GeV, assuming $\langle \sigma v \rangle = 3 \times 10^{-26}$ cm^3 s^{-1}. In addition, we used these values to compare the electron plus positron flux from LKP annihilation with recent observational electron plus positron data, which indicate the light LKP, such as $m_{B^{(1)}} = 300$ GeV, might be excluded, since the edge–like structure has not been observed yet.

In addtion, the obtained upper limits on B_f assuming the coefficient C_B and index Γ_B for the power-law background flux based on the HESS observation are given in Table 4. The HESS observational data is obtained by the gamma-ray emission around the Galactic center, but the value of B_f to fit the positron fraction is derived by the observation of the electrons and positrons produced by annihilation of LKP far from the Galactic center. Thus we may not be able to directly compare the constraints on B_f by gamma-ray emission with electrons and positrons. However, if we simply discuss for these values, the values of B_f derived from the positron fraction fit to the AMS-02 data at 100 GeV might be excluded by HESS observation. This indicates that LKP could not be a good candidate of the Galactic dark matter which is responsible for the positron excess observed by AMS–02, and requires other explanation, such as other types of dark matter particles or astrophysical sources.

This paper also estimated the accessible range of the boost factor using a maximum likelihood analysis. If the observed energy range for gamma-rays extends to lower energies, the accessible range of the boost factor will be lowered since more continuum events will be detected. Assuming the detector having effective area of 1000 cm^2, if the signal is not detected in 10 years observation, the upper limit of the factor is about 3×10^4 for $m_{B^{(1)}} = 800$ GeV if only taking data near the peak into account. Furthermore, if $m_{B^{(1)}}$ is light or the energy resolution of the detector is good (say the order of 0.5%), we may tightly constrain the factor (down to about 2).

In addition, if we can detect the LKP signal with 0.5% energy resolution detector, we would see the characteristic structure around the $m_{B^{(1)}}$, as is shown in Fig. 23, when large number of photons are detected.

If the characteristic structure in gamma-ray and/or electron plus positron flux is observed by new and future missions, like CALET [87], DAMPE [110] and GAMMA-400 [111], we may conclude dark matter is made of LKP. It would be a conclusive evidence for the existence of extra dimensions.

Acknowledgments

Firstly, I would like to be deeply grateful my supervisor Professor Masaki Mori for supporting and encouraging my research and for growing me as a scientist. I also would like to really thank Professor Yuji Sugawara for his guidance and advice. In addition, I would like to quite thank Hiroshi Kuratsuji for his tremendous mentor. Also, I would like to thank Yutaka Fujita for useful advice.

Secondly, I would like to thank Akihiko Kawamura and Fumihiro Matsui for useful discussions and partnership. In addition, I would like to be grateful Takahiro Uetoko, Mai Yashiki, Takafumi Okubo, Taiki Wada, Takenori Ishii, and a lot of people for helpful comments.

Finally, I should especially thank my family, Ko Tsuchida, Mieko Tsuchida, Misa Hiramatsu, Masashi Hiramatsu, and Hina Hiramatsu. Words cannot express how grateful I am to my family.

References

[1] F. Zwicky, "Die Rotverschiebung von extragalaktischen Nebeln," Helv. Phys. Acta. **6**, 110 (1933).

[2] Y. Sofue and V. Rubin, "Rotation curves of spiral galaxies," Annual Review of Astron. Astrophys. **39**, 1 (2001).

[3] V. Rubin, W. K. Ford, and N. Thonnard, "EXTENDED ROTATION CURVES OF HIGH-LUMINOSITY SPIRAL GALAXIES. IV. SYSTEMATIC DYNAMICAL PROPERTIES, Sa $\rightarrow$ Sc" Astrophys. J **225**, L107 (1978).

[4] For a review, See, e.g., G. Bertone, D. Hooper, and J. Silk, "Particle dark matter: evidence, candidates and constraints," Phys. Rep. **405**, 279 (2005).

[5] M. Milgrom, "A Modification of the Newtonian dynamics as a possible alternative to the hidden mass hypothesis," Astrophys. J. **270**, 365 (1983).

[6] S. S. McGaugh, "A Tale of Two Paradigms: the Mutual Incommensurability of ΛCDM and MOND," arXiv:1204.7525 [astro-ph.CO] (2014).

[7] C. Alcock *et al.* (MACHO Collaborations), "The MACHO Project: Microlensing Results from 5.7 Years of LMC Observations," Astrophys. J. **542**, 281 (2000).

[8] P. A. R. Ade *et al.*, "Planck 2013 results. XVI. Cosmological parameters," Astron. Astrophys. **571**, A16 (2014).

[9] Y. Fukuda *et al.* (Super-Kamiokande Collaboration), "Evidence for Oscillation of Atmospheric Neutrinos," Phys. Rev. Lett. **81**, 1562 (1998).

[10] S. D. White, C. Frenk, and M. Davis, "Clustering in a Neutrino Dominated Universe," Astrophys. J. **274**, L1 (1983).

[11] G. B. Gelmini, "TASI 2014 LECTURES: THE HUNT FOR DARK MATTER," arXiv:hep-ph/1502.01320 (2015).

[12] L. Bergström, "Dark matter candidates," New J. Phys. **11**, 105006 (2009).

[13] J. Wess, B. Zumino, "A lagrangian model invariant under supergauge transformations," Phys. Lett. B **49**, 52 (1974).

[14] S. P. Martin, "A Supersymmetry Primer," arXiv:hep-ph/9709356 (1997).

[15] S. Chatrchyan *et al.* (CMS Collaboration), "Search for Supersymmetry at the LHC in Events with Jets and Missing Transverse Energy," Phys. Rev. Lett. **107**, 221804 (2011).

[16] G. Aad *et al.* (ATLAS Collaboration), "Search for squarks and gluinos using final states with jets and missing transverse momentum with the ATLAS detector in $\sqrt{s} = 7$ TeV proton-proton collisions," Phys. Lett. B **710**, 67 (2012).

[17] H. C. Cheng, K. T. Matchev, and M. Schmaltz, "Radiative corrections to Kaluza-Klein masses," Phys. Rev. D **66**, 036005 (2002).

[18] L. Bergström, T. Bringmann, M. Eriksson, and M. Gustafsson, "Gamma-Rays from Kaluza-Klein dark matter," Phys. Rev. Lett. **94**, 131301 (2005).

[19] J. F. Navarro, C.S. Frenk, and S. D. White, "The structure of Cold Dark Matter Halos," Astrophys. J. **462**, 563 (1996).

[20] M. Weber and W. de Boer, "Determination of the local dark matter density in our Galaxy" Astron. Astrophys. **509**, A25 (2010).

[21] F. Prada, A. Klypin, J. Flix, M. Martinez, and E. Simonneau, "Dark Matter Annihilation in the Milky Way Galaxy: Effects of Baryonic Compression," Phys. Rev. Lett. **93**, 241301 (2004).

[22] S. Torii, "Calorimetric electron telescope mission Search for dark matter and nearby sources," Nucl. Instrum. Methods. A **630**, 55 (2011).

[23] M. Mori *et al.*, "Expected Performance of CALET as a High Energy Gamma Rry Observatory," Proc. 33rd ICRC (Rio de Janeiro), Paper 0248 (2013).

[24] S. Tsuchida and M. Mori, "The observability of gamma-ray spectral features from Kaluza-Klein dark matter annihilation," Proc. 34th ICRC (The Hague), PoS (ICRC2015) 1180.

[25] S. Tsuchida and M. Mori, "The electron plus positron spectrum from annihilation of Kaluza-Klein dark matter in the Galaxy," Under Submission for Publication.

[26] G. Jungman *et al.*, "Supersymmetric dark matter," Phys. Rep. **267**, 195 (1996).

[27] G. Servant and T.M.P. Tait, "Is the lightest Kaluza-Klein particle a viable dark matter candidate?," Nucl. Phys. B **650**, 391 (2003).

[28] X. J. Bi, P. F. Yui, and Q. Yuan, "Status of Dark Matter Detection," arXiv:1409.4590 [hep-ph] (2014).

[29] T. Saab, "An Introduction to Dark Matter Direct Detection Searches & Techniques," arXiv:1203.2566 [physics.ins-det] (2012).

[30] Particle Data Group 2014: K. A. Olive *et al.*, "Review of Particle Physics," Chinese Physics C, 38, 090001 (2014).

[31] R. Bernabei *et al.* (DAMA collaboration), "First results from DAMA/LIBRA and the combined results with DAMA/NaI," Eur. Phys. J. **C56**, 333 (2008).

[32] H. S. Lee *et al.* (KIMS collaboration), "Limits on Interactions between Weakly Interacting Massive Particles and Nucleons Obtained with CsI(Tl) Crystal Detectors," Phys. Rev. Lett **99**, 091301 (2007).

[33] Z. Ahmed *et al.* (CDMS-II collaboration) "Dark Matter Search Results from the CDMS II Experiment," Science **327**, 1619 (2010).

[34] E. Armengaud *et al.* (EDELWEISS collaboration), "Final results of the EDELWEISS-II WIMP search using a 4-kg array of cryogenic germanium detectors with interleaved electrodes," Phys. Lett. **B702**, 329 (2011).

[35] C. E. Aalseth *et al.* (CoGeNT collaboration), "Results from a Search for Light-Mass Dark Matter with a p-Type Point Contact Germanium Detector," Phys. Rev. Lett. **106**, 131301 (2011).

[36] G. Angloher *et al.*, "Results from 730 kg days of the CRESST-II Dark Matter search," Eur. Phys. J. **C72**, 1971 (2012)

[37] E. Aprile *et al.* (XENON100 collaboration), "Dark Matter Results from 225 Live Days of XENON100 Data," Phys. Rev. Lett. **109**, 181301 (2012).

[38] D. Y. Akimov *et al.*, "WIMP-nucleon cross-section results from the second science run of ZEPLIN-III," Phys. Lett. **B709**, 14 (2012).

[39] Z. Li *et al.*, "The Cryogenic System for the Panda-X Dark Matter Search Experiment," arXiv:1207.5100 [astro-ph.IM] (2012).

[40] K. Abe *et al.*, "XMASS detector," Nucl. Instrum. Meth. **A716** (2013) 78.

[41] E. Behnke *et al.* (COUPP collaboration), "First dark matter search results from a 4-kg CF3I bubble chamber operated in a deep underground site," Phys. Rev. D **86**, 052001 (2012).

[42] S. Archambault *et al.* (PICASSO collaboration), "Constraints on low-mass WIMP interactions on ^{19}F from PICASSO," Phys. Lett. **B711**, 153 (2012).

[43] M. Felizardo *et al.* (SIMPLE collaboration), "Final Analysis and Results of the Phase II SIMPLE Dark Matter Search," Phys. Rev. Lett. **108**, 201302 (2012).

[44] F. Aharonian *et al.*, "Probing the ATIC peak in the cosmic-ray electron spectrum with H.E.S.S.," Astron. Astrophys. **508**, 561-564 (2009).

[45] See, e.g., J. A. R. Cembranos, V. Gammaldi, and A. L. Maroto, "Possible dark matter origin of the gamma ray emission from the Galactic Center observed by HESS," Phys. Rev. D **86**, 103506 (2012) and references therein.

[46] F. Aharonian *et al.* (HESS Collaboration), "HESS Observations of the Galactic Center Region and Their Possible Dark Matter Interpretation," Phys. Rev. Lett. **97**, 221102 (2006).

[47] P. L. Nolan *et al.*, "Fermi Large Area Telescope second source catalog," Astrophys. J. Suppl. Ser. **199**, 31 (2012).

[48] M. Chernyakova, D. Malyshev, F. A. Aharonian, R. M. Crocker, and D. I. Jones, "THE HIGH-ENERGY, ARCMINUTE-SCALE GALACTIC CENTER GAMMA-RAY SOURCE," Astrophys. J. **726**, 60 (2011).

[49] T. Bringmann, X. Huang, A. Ibarra, S. Vogl, and C. Weniger, "Fermi LAT Search for Internal Bremsstrahlung Signatures from Dark Matter Annihilation," J. Cosmol. Astropart. Phys. **07**, 054 (2012).

[50] D. P. Finkbeiner, M. Su, and C. Weniger, "Is the 130 GeV Line Real? A Search for Systematics in the Fermi-LAT Data," J. Cosmol. Astropart. Phys. **01**, 029 (2013).

[51] M. Su and D. P. Finkbeiner, "STRONG EVIDENCE FOR GAMMA-RAY LINE EMISSION FROM THE INNER GALAXY," arXiv:1206.1616v2 [astro-ph.HE] (2012).

[52] C. Weniger, "Tentative observation of a gamma-ray line at the Fermi-LAT," J. Cosmol. Astropart. Phys. **08**, 007 (2012).

[53] M. Ackermann *et al.* (Fermi-LAT collaboration), "Fermi LAT search for dark matter in gamma-ray lines and the inclusive photon spectrum," Phys. Rev. D **86**, 022002 (2012).

[54] M. Ackermann *et al.* (Fermi-LAT collaboration), "Search for gamma-ray spectral lines with the Fermi Large Area Telescope and dark matter implications," Phys. Rev. D **88**, 082002 (2013).

[55] O. Adriani *et al.* (PAMELA collaboration), "Cosmic-Ray Positron Energy Spectrum Measured by PAMELA," Phys. Rev. Lett. **111** 081102 (2013).

[56] M. Ackermann *et al.*, "Measurement of Separate Cosmic-Ray Electron and Positron Spectra with the Fermi Large Area Telescope," Phys. Rev. Lett. **108**, 011103 (2012);

[57] M. Aguilar *et al.* (AMS collaboration), "First Result from the Alpha Magnetic Spectrometer on the International Space Station: Precision Measurement of the Positron Fraction in Primary Cosmic Rays of 0.5-350 GeV," Phys. Rev. Lett. **110**, 141102 (2013); See also its Supplemental Material.

[58] J. Chang *et al.*, "An excess of cosmic ray electrons at energies of 300-800 GeV," Nature **456** (2008) 362.

[59] S. Torii *et al.*, "THE ENERGY SPECTRUM OF COSMIC-RAY ELECTRONS FROM 10 TO 100 GeV OBSERVED WITH A HIGHLY GRANULATED IMAGING CALORIMETER," Astrophys. J **559**, 973-984 (2001).

[60] I. Cholis and D. Hooper, "Dark matter and pulsar origins of the rising cosmic ray positron fraction in light of new data from the AMS," Phys. Rev. D **88**, 023013 (2013); T. Linden and S. Profumo, "PROBING THE PULSAR ORIGIN OF THE ANOMALOUS POSITRON FRACTION WITH AMS-02 AND ATMOSPHERIC CHERENKOV TELESCOPES," Astrophys. J. **772**, 18 (2013) and references therein.

[61] Y. Fujita *et al.*, "Is the PAMELA anomaly caused by supernova explosions near the Earth?," Phys. Rev. D **80**, 063003 (2009); K. Kohri *et al.*, "Can we explain AMS-02 antiproton and positron excesses simultaneously by nearby supernovae without pulsars nor dark matter?," arXiv:1505.01236 [astro-ph.HE] (1015) and references therein.

[62] AMS-02 Collaborations, talks given at the *AMS Days at CERN*, 15-17 April, 2015 (2015).

[63] G. Giesen *et al.*, "AMS-02 antiprotons, at last! Secondary astrophysical component and immediate implications for Dark Matter," J. Cosmol. Astropart. Phys. **09**, 023 (2005).

[64] H. B. Jin *et al.*, "Upper limits on dark matter annihilation cross sections from the first AMS-02 antiproton data," Phys. Rev. D **92**, 055027 (2015).

[65] T. Tanaka *et al.* (The Super-Kamiokande Collaboration), "AN INDIRECT SEARCH FOR WEAKLY INTERACTING MASSIVE PARTICLES IN THE SUN USING 3109.6 DAYS OF UPWARD-GOING MUONS IN SUPER-KAMIOKANDE," Astrophys. J. **742**, 78 (2011).

[66] J. D. Zornoza *et al.* (ANTARES collaboration), "Results and prospects of dark matter searches with ANTARES," Nucl. Instrum. Meth. **A742**, 173 (2014)

[67] M. G. Aartsen *et al.* (IceCube collaboration), "Search for Dark Matter Annihilations in the Sun with the 79-String IceCube Detector," Phys. Rev. Lett. **110**, 131302 (2013).

[68] R. Abbasi *et al.* (IceCube collaboration), "Search for Neutrinos from Annihilating Dark Matter in the Direction of the Galactic Center with the 40-String IceCube Neutrino Observatory," arXiv:1210.3557v3 [hep-ex] (2013).

[69] K. D. Hoffman, "High energy neutrino telescopes," New. J. Phys. **11**, 055006 (2009).

[70] T. Kaluza, "On The Problem Of Unity In Physics," Sitzungsber. Press. Akad. Wiss. Berlin **K1**, 966 (1921).

[71] O. Klein, "Quantum Theory And Five-Dimensional Theory Of Relativity," Z. Phys. **37**, 895 (1926).

[72] T. Appelquist, H. C. Cheng, B. A. Dobrescu "Bound on Universal Extra Dimensions," Phys. Rev. D **64**, 035002 (2001).

[73] D. Hooper, "TASI 2008 Lectures on Dark Matter," arXiv:0901.4090 [hep-ph] (2009).

[74] L. Bergström, T. Bringmann, M. Eriksson, and M. Gustafsson, "Two photon annihilation of Kaluza-Klein dark matter," J. Cosmol. Astropart. Phys. **04**, 004 (2005).

[75] D. Hooper and G. D. Kribs, "Probing Kaluza-Klein dark matter with neutrino telescopes," Phys. Rev. D **67** (2003) 055003.

[76] N. Fornengo, L. Pieri, and S. Scopel, "Neutralino annihilation into gamma rays in the Milky Way and in external galaxies," Phys. Rev. D **70**, 103529 (2004).

[77] T. Bringmann and C. Weniger, "Gamma-ray signals from dark matter: Concepts, status, prospects," Physics of Dark Universe **1**, 194 (2012).

[78] A. Cesarini, F. Fucito, A. Lionetto, A. Morselli, and P. Ullio, "The Galactic center as a dark matter gamma-ray source," Astropart. Phys. **21**, 267 (2004).

[79] N. Arkani-Hamed, D. P. Finkbeiner, T. R. Slatyer, and N. Weiner, "A theory of dark matter," Phys. Rev. D **79**, 015014 (2009).

[80] M. Ibe, H. Murayama, and T. T. Yanagida, "Breit-Wigner enhancement of dark matter annihilation," Phys. Rev. D **79**, 095009 (2009).

[81] A. A. Abdo *et al.* (Fermi-LAT collaboration), "OBSERVATIONS OF MILKY WAY DWARF SPHEROIDAL GALAXIES WITH THE FERMI-LARGE AREA TELESCOPE DETECTOR AND CONSTRAINTS ON DARK MATTER MODELS," Astrophys. J. **712**, 147 (2010).

[82] F. Aharonian *et al.*, "Observations of the Sagittarius dwarf galaxy by the HESS experiment and search for a dark matter signal," Astropart. Phys. **29**, 55 (2008); Erratum Astropart. Phys. **33**, 274 (2010).

[83] F. Aharonian *et al.*, "Spectrum and variability of the Galactic center VHE γ-ray source HESS J1745-290," Astron. Astrophys. **503**, 817 (2009).

[84] J. R. Mattox *et al.*, "The Likelihood analysis of EGRET data," Astrophys. J. **461**, 396 (1996).

[85] H. C. Cheng, J. L. Feng, and K. T. Matchev, "Kaluza-Klein Dark Matter," Phys. Rev. Lett. **89**, 211301 (2002).

[86] A. A. Moiseev *et al.*, "SEARCHING FOR KALUZA-KLEIN DARK MATTER SIGNATURES IN THE LAT ELECTRON FLUX," Frascati Physics Series **VVV**, 1 (2007).

[87] S. Torii for the CALET collaboration, "The CALorimetric Electron Telescope (CALET): High Energy Astroparticle Physics Observatory on the International Space Station," Proc. 34th ICRC (The Hague), PoS (ICRC2015) 581.

[88] M. Cirelli *et al.*, "PPPC 4 DM ID: a poor particle physicist cookbook for dark matter indirect detection," J. Cosmol. Astropart. Phys. **1103**, 051. (2011) Erratum: J. Cosmol. Astropart. Phys. **1210**, E01 (2012).

[89] P. Ciafaloni *et al.*, "Weak corrections are relevant for dark matter indirect detection," J. Cosmol. Astropart. Phys. **1103**, 019 (2011).

[90] I. V. Moskalenko and A. W. Strong, "Positrons from particle dark-matter annihilation in the Galactic halo: Propagation Green ' s functions," Phys. Rev. D **60**, 063003 (1999).

[91] J. Buch *et al.*, "PPPC 4 DM secondary: a Poor Particle Physicist Cookbook for secondary radiation from Dark Matter," J. Cosmol. Astropart. Phys. **09**, 037 (2015).

[92] G. R. Blumenthal, R. J. Gould, "Bremsstrahlung, Syncrotron Radiation, and Compton Scattering of High Energy Electrons Traversing Dilute Gases," Rev. Mod. Phys. **42**, 237 (1970).

[93] T. Stanev, "*High Energy Cosmic Rays*," Springer Verlag (2003).

[94] Q. Yuan and X. J. Bi, "Reconcile the AMS-02 positron fraction and Fermi-LAT/HESS total e ± spectra by the primary electron spectrum hardening," Phys. Lett. **B727**, 1 (2013).

[95] M. Boudard *et al.*, "A fussy revisitation of antiprotons as a tool for Dark Matter searches," J. Cosmol. Astropart. Phys. **05**, 013 (2015).

[96] O. Adriani *et al.*, "A statistical procedure for the identification of positrons in the PAMELA experiment," Astropart. Phys. **34**, 1 (2010).

[97] R. L. Golden *et al.*, "Observations of cosmic-ray electrons and positrons using an imaging calorimeter," Astrophys. J **436**, 769-775 (1994).

[98] R. L. Golden *et al.*, "A measurement of the absolute flux of cosmic-ray electrons," Astrophys. J **287**, 622-632 (1984).

[99] K. -K. Tang, "The energy spectrum of electrons and cosmic-ray confinement: A new measurement and its interpretation," Astrophys. J **278**, 881-892 (1984).

[100] M. Boezio *et al.*, "THE COSMIC-RAY ELECTRON AND POSITRON SPECTRA MEASURED AT 1 AU DURING SOLAR MINIMUM ACTIVITY," Astrophys. J **532**, 653-669 (2000).

[101] M. A. DuVernois *et al.*, "COSMIC-RAY ELECTRONS AND POSITRONS FROM 1 TO 100 GeV: MEASUREMENTS WITH HEAT AND THEIR INTERPRETATION," Astrophys. J **559**, 296-303 (2001).

[102] M. Aguilar *et al.*, "The Alpha Magnetic Spectrometer (AMS) on the International Space Station: Part I — results from the test flight on the space shuttle," Phys. Rep. **366**, 331-405 (2002).

[103] S. Torii *et al.*, "High-energy electron observations by PPB-BETS flight in Antarctica," arXiv:0809.0760 [astro-ph]; K. Yoshida *et al.*, "Cosmic-ray electron spectrum above 100 GeV from PPB-BETS experiment in Antarctica," Adv. Sp. Res. **42**, 1670-1675 (2008).

[104] T. Kobayashi *et al.*, "OBSERVATIONS OF HIGH-ENERGY COSMIC-RAY ELECTRONS FROM 30 GeV TO 3 TeV WITH EMULSION CHAMBERS," Astrophys. J **760**, 146 (2012).

[105] S. Ting, Talk at the *33rd International Cosmic Ray Conference*, (Rio de Janeiro), 2-9 July 2013 (2013).

[106] M. Ackermann *et al.* (Fermi LAT collaboration), "Fermi LAT observations of cosmic-ray electrons from 7 GeV to 1 TeV," Phys. Rev. D **82**, 092004 (2010).

[107] O. Adriani *et al.*, "Cosmic-Ray Electron Flux Measured by the PAMELA Experiment between 1 and 625 GeV," Phys. Rev. Lett. **106**, 201101 (2011).

[108] L. Bergström *et al.*, "Investigating Gamma-Ray Lines from Dark Matter with Future Observatories," J. Cosmol. Astropart. Phys. **11**, 025 (2012).

[109] T. Bringmann *et al.*, "On the Relevance of Sharp Gamma-Ray Features for Indirect Dark Matter Searches," Phys. Rev. D **84**, 103525 (2011).

[110] V. Galio *et al.*, "The test results of the Silicon Tungsten Tracker of DAMPE," Proc. 34th ICRC (The Hague), PoS (ICRC2015) 1199.

[111] N. P. Topchiev *et al.*, "GAMMA-400 gamma-ray observatory," Proc. 34th ICRC (The Hague), PoS (ICRC2015) 1026.